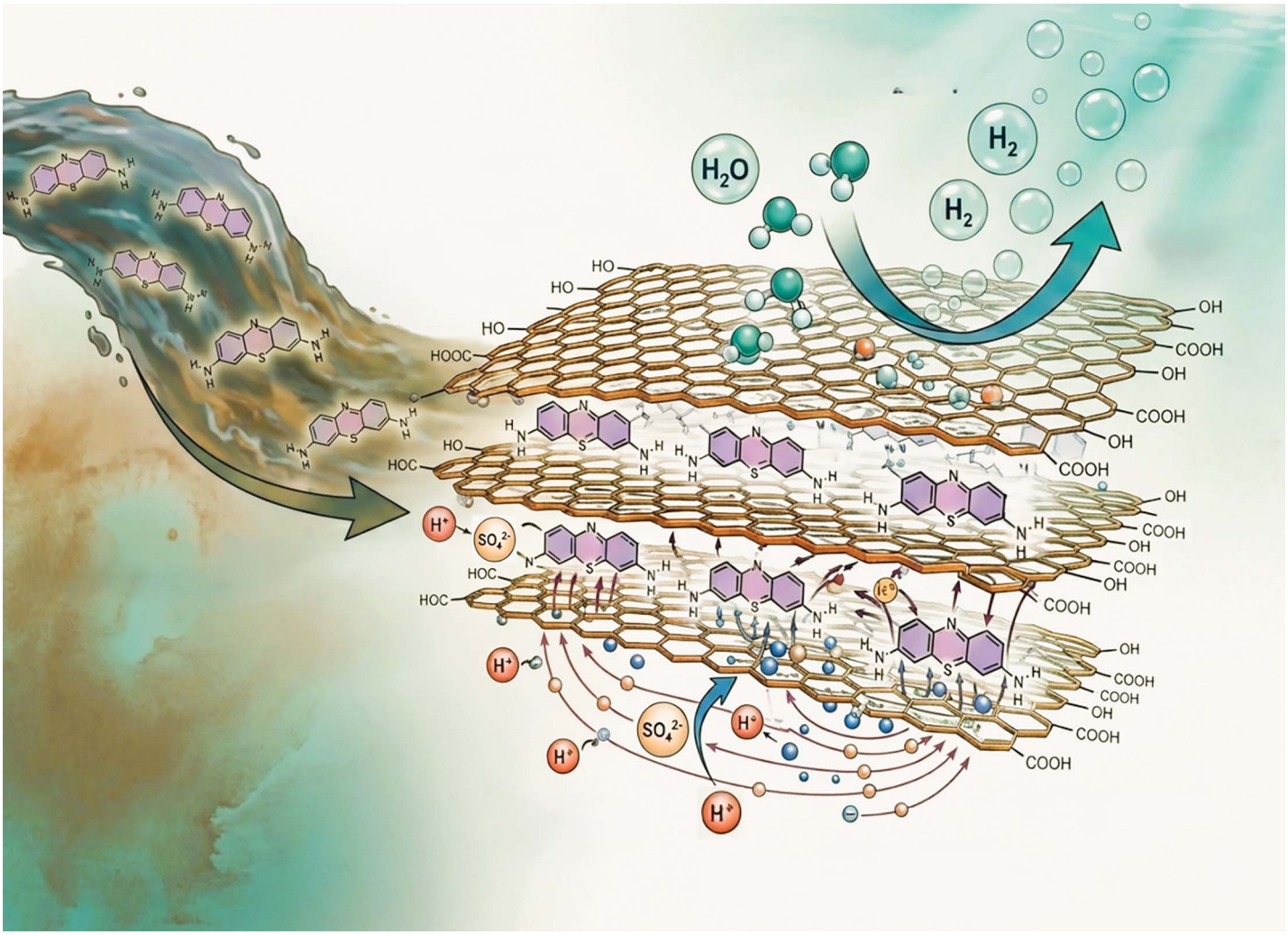

Showcasing research from Dr Ehab N. El Sway's lab (NanoElectrochemistry Lab), Department of Chemistry, School of Sciences and Engineering, The American University in Cairo, Egypt.

Graphene oxide nanoribbons grafted with thionine as versatile materials for energy storage and hydrogen evolution electrocatalysis

This work addresses global environmental and energy challenges by immobilizing toxic thionine dye onto graphene oxide nanoribbons (GONRs) to create a high-performance, multifunctional composite. Through hydrothermal and room-temperature synthesis, this research developed eco-friendly electrodes that simultaneously tackle dye remediation and advanced energy storage and conversion. The room-temperature composite achieved an impressive specific capacitance of 732 F g^{-1}, maintaining over 100% stability after 10 000 cycles, while the hydrothermal variant demonstrated efficient hydrogen evolution with a low overpotential of 122 mV. This dual-purpose material marks a significant step forward in integrating wastewater treatment with sustainable energy storage and green fuel generation.

Image reproduced by permission of Ehab El Sawy from *Nanoscale Adv.*, 2026, **8**, 2908. Image created with Google Gemini.

As featured in:

See Ehab N. El Sawy *et al.*, *Nanoscale Adv.*, 2026, **8**, 2908.

ROYAL SOCIETY OF CHEMISTRY

rsc.li/nanoscale-advances

Registered charity number: 207890

Nanoscale Advances

ROYAL SOCIETY OF CHEMISTRY

PAPER

View Article Online
View Journal | View Issue

Cite this: *Nanoscale Adv.*, 2026, **8**, 2908

Graphene oxide nanoribbons grafted with thionine as versatile materials for energy storage and hydrogen evolution electrocatalysis

Asmaa R. Heiba, †[a] M. O. Abdel-Salam †[abc] and Ehab N. El Sawy *[a]

Wastewater treatment, energy storage, and green fuel generation remain among the most pressing global challenges. In this work, environmental remediation and energy conversion are addressed simultaneously by immobilizing the toxic dye thionine onto graphene oxide nanoribbons (GONRs) to create a functional composite for advanced energy applications. The GONRs/thionine materials were synthesized *via* hydrothermal (HT) and room-temperature (RT) routes and systematically characterized using SEM, TEM, XRD, UV-vis spectroscopy, FT-IR, Raman spectroscopy, and XPS. Their electrochemical performance for supercapacitor and hydrogen evolution reaction (HER) applications was evaluated through CV, GCD, EIS, LSV, and CP measurements. For supercapacitor applications, thionine-functionalized GONRs demonstrated a marked enhancement in capacitance in 1 M H_2SO_4 arising from thionine-induced pseudocapacitance. GONRs/Th (RT) exhibited a specific capacitance of 732 F g^{-1} at 1 A g^{-1} in a three-electrode setup. A symmetric two-electrode device made from GONRs/Th (RT) reached a capacitance of 141 F g^{-1} at 1 A g^{-1} within a 1.7 V window, delivering a maximum energy density of 57 Wh kg^{-1} and a power density of 8.305 kW kg^{-1} and retaining 102% after 10 000 cycles. In the HER, GONRs/Th (HT) showed an overpotential of 122 mV at 10 mA $^{-1}cm^{-2}$ and a Tafel slope of 91 mV dec^{-1}, highlighting its potential as a versatile, eco-friendly electrode material.

Received 13th January 2026
Accepted 18th February 2026

DOI: 10.1039/d6na00029k

rsc.li/nanoscale-advances

1. Introduction

Dependence on fossil fuels endangers environmental stability and worsens the effects of climate change,[1–3] driving intensive research into storage technologies and clean fuel production.[4,5] Two key approaches are electrochemical energy storage in supercapacitors (SCs) and renewable fuel production through water electrolysis. Supercapacitors (SCs) are gaining attention as an effective energy storage option due to their rapid charge–discharge performance and durable cycling.[6,7] SCs can deliver rapid energy surges, making them suitable for applications that demand high power for short periods.[8] In parallel, green hydrogen production *via* water electrolysis provides a complementary pathway to store renewable energy as a transferable fuel, making it a crucial technology for future green fuel production.[9] However, conventional devices for both technologies rely on scarce and costly materials.

Organic-based electrode materials offer a viable alternative owing to their abundant availability, customizable structures, and environmental sustainability.[10,11] Among organic molecules, *n*-type molecules containing azo (N=N),[12,13] carbonyl (C=O),[14–16] nitro (–NO_2),[17] imine (C=N),[18] or sulfide (–S–S–)[19] groups deliver fast kinetics, high capacities, and favorable redox potentials.[20,21] However, they often suffer from poor conductivity and electrolyte dissolution.[10] To address this, particular attention has been given to thionine, a phenothiazine-based dye that combines C=S and C=N redox-active sites, offering high reversibility, a broad pH-dependent voltage window, a theoretical capacity of ≈ 235 mAh g^{-1}, and suitable active sites for the HER.[8,22,23] Yet, its environmental toxicity and instability limit direct application.[24] Embedding thionine in inorganic matrices can address these challenges by forming robust organic–inorganic hybrid systems through covalent and/or π–π interactions.[25]

Although carbon-based electrodes have low energy density due to their stacking and relatively low surface area, they are remarkably chemically and thermally stable and highly conductive, making them an excellent choice as inorganic matrices.[26–28] In carbon electrodes, the primary mechanism for charge storage is electric double-layer (EDL) capacitance, with pseudocapacitance playing a minor role. Multi-walled carbon nanotubes (MWCNTs) are increasingly considered for supercapacitor applications due to their excellent conductivity,

[a]*Department of Chemistry, School of Sciences and Engineering, the American University in Cairo, Cairo, 11835, Egypt. E-mail: ehab.elsawy@aucegypt.edu*
[b]*Analysis and Evaluation Department, Egyptian Petroleum Research Institute (EPRI), 1 Ahmed El Zomor St., Nasr City, Cairo, 11727, Egypt*
[c]*Central Analytical Laboratories, Nanotechnology Research, Egyptian Petroleum Research Institute (EPRI), 1 Ahmed El Zomor St., Nasr City, Cairo, 11727, Egypt*
† Authors contributed equally to this work.

chemical stability, and well-organized nanostructure.[27] However, their rope-like aggregation restricts ion transport, mainly inside the tubes, thereby limiting capacitance.[29] A rational modification to overcome these limitations is the unzipping of MWCNTs into graphene oxide nanoribbons (GONRs), which produces shorter, more accessible nanostructures with improved electrochemical performance.[30] GONRs combine ultra-high conductivity ($\sim 10^4$ S cm^{-1}) with stronger pseudocapacitive behavior and a higher volume-specific capacity than MWCNTs.[31] In addition, the abundant –OH/–COOH groups on GONRs' surfaces serve as excellent anchoring points for organic molecules, enabling the construction of composite materials that can inhibit the spontaneous restacking of GONR sheets.[32] The negatively charged GONR surface further promotes electrostatic adsorption of cationic dyes like thionine, while –COOH edge groups can form stable amide bonds with their –NH_2 groups. Incorporating thionine thus both suppresses GONR restacking and prevents thionine dissolution, yielding hybrid electrodes for supercapacitor application with higher capacity, improved cycling stability, and reduced environmental risks.

Beyond energy storage, such functionalization strategies are equally critical for electrocatalysis. In this context, carbon materials doped with nitrogen and sulfur have attracted interest due to their enhanced performance in the hydrogen evolution reaction (HER).[33,34] Doping carbon with nitrogen, sulfur, or both modifies its electronic structure, improving conductivity and generating abundant active sites, thereby increasing catalytic activity. N, S-co-doped carbons exhibit a lower onset potential, improved kinetics, and stability, with reported Tafel slopes as low as $\sim$57 mV dec^{-1}.[35] Inspired by these advances, we designed a hybrid material by grafting thionine molecules onto graphene oxide nanoribbons (GONRs) to combine the merits of organic molecules with the conductive properties of carbon matrices. This approach integrates C=N and C=S redox-active groups from thionine into the carbon matrix, enabling a detailed examination of their effects on the electrocatalytic performance of GONRs in the hydrogen evolution reaction (HER). Ultimately, this method offers a versatile platform for developing advanced energy storage systems and electrocatalysts for sustainable hydrogen production.

Accordingly, in this work, we synthesized a novel GONRs/Th composite *via* one-step physical mixing at room temperature and under hydrothermal conditions, aiming to design an organic-inorganic hybrid electrode material that is efficient for both HER electrocatalysis and supercapacitor applications. The GONRs/Th composite was examined using various physical and chemical techniques to verify the attachment of thionine to the GONR surface and to detect differences in properties resulting from different synthesis methods, thereby facilitating better correlation between the electrochemical behavior and the composite. The electrochemical evaluation of the GONRs/Th composites revealed enhanced supercapacitor properties relative to pure GONRs, particularly for the GONRs/Th (RT) variant, which exhibited significantly higher specific capacitance and greater energy storage capacity. Additionally, the GONRs/Th (HT) composite exhibited remarkable electrocatalytic activity for the hydrogen evolution reaction (HER), with notably lower overpotential and Tafel slope than both the GONRs/Th (RT) and the original GONRs. By attaching thionine to GONRs through an amide bond, we established an effective conductive network that facilitates electron and ion transport, strengthens the interaction between organic and inorganic parts, and offers stable, efficient active sites for HER catalysis.

2. Experimental work

2.1. Materials

The initial material, multi-walled carbon nanotubes (MWCNTs), was sourced from the Egyptian Petroleum Research Institute (EPRI) located in Cairo, Egypt. These nanotubes have outer diameters of 20–40 nanometers and were produced by chemical vapor deposition (CVD). The chemicals involved included hydrogen peroxide (H_2O_2, 30%, Merck), sulfuric acid (H_2SO_4, 98%, Sigma-Aldrich), potassium permanganate ($KMnO_4$, Sigma-Aldrich), hydrochloric acid (HCl, 30%, Merck), potassium hydroxide (KOH pellets, Sigma-Aldrich, >85%), and thionine ($C_{12}H_{10}N_3S^+$, Sigma-Aldrich). Dialysis tubing (Product No. D9402) and 0.45 μm nylon membranes from Sigma-Aldrich were used. All procedures used purified water with resistivity exceeding 18.3 MΩ cm.

2.2. Production of GONRs

GONRs were produced by oxidative unzipping of MWCNTs, an approach adapted from the study by D. Kosynkin *et al.*[30,36] Briefly, 0.3 g of multi-walled carbon nanotubes (MWCNTs) were dispersed in concentrated sulfuric acid (120 mL) and stirred at ambient temperature for 24 hours. Subsequently, 1.5 g of potassium permanganate ($KMnO_4$) was added gradually while maintaining the temperature below 20 °C. After cooling the mixture in an ice bath, 400 mL of deionized water was slowly introduced, followed by vigorous stirring for 30 minutes to dilute the mixture. The solution was subsequently heated to 85 °C and continuously stirred for a further 4 hours. To inhibit insoluble manganese dioxide (MnO_2) formation, 60 mL of 30% hydrogen peroxide (H_2O_2) was added, along with deionized water (200 mL), before the washing step. The graphene oxide nanoribbons (GONRs) were purified by sequential washes with 10% hydrochloric acid until the solution approached a neutral pH, followed by rinsing with deionized water. The suspension was either used directly to fabricate composites and conduct electrochemical tests to prevent GONR stacking, or it was filtered through a 0.45 μm nylon membrane, washed with ethanol and water, and then vacuum-dried at 60 °C for subsequent physical characterization.

2.3. Synthesis of GONRs/Th composites

The GONRs/Th composites were synthesized *via* physical mixing of GONRs and Th at room temperature (RT) or mixing at RT followed by hydrothermal treatment (HT). For the physical mixing process at room temperature, 25 mL of a GONR suspension (1 mg mL^{-1}) was combined with 13.6 mg of Th, which was incorporated into the dispersion (Scheme 1). The

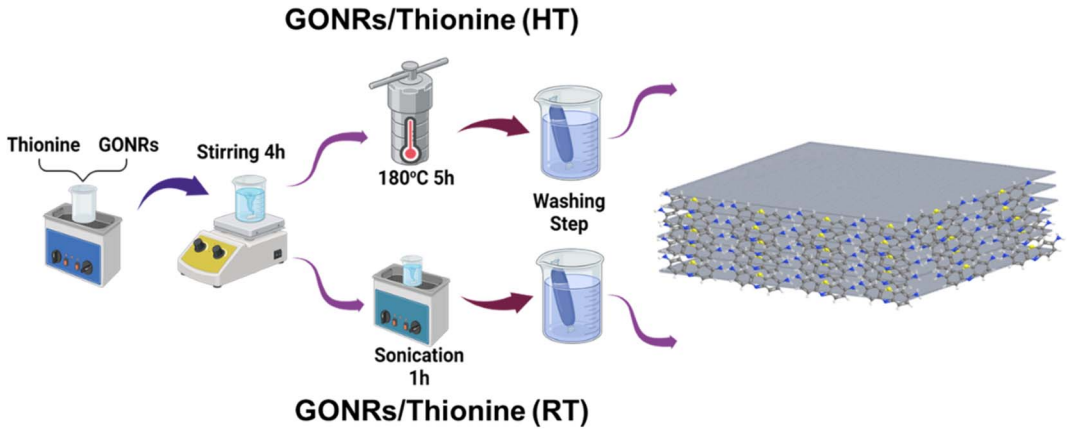

Scheme 1 Illustration for preparing GONRs/Th (RT and HT).

solution was stirred continuously for 4 hours, followed by 1 hour of sonication at ambient temperature to promote thionine integration into the GONR layers.

For hydrothermal processing, a GONRs/Th solution prepared earlier was placed in a sealed autoclave (Teflon-lined stainless steel), heated to 180 °C for 5 hours, and then cooled to room temperature naturally. The resulting GONRs/Th composites were purified by transferring the final solution into a dialysis membrane, which was then immersed in deionized water and rinsed thoroughly to eliminate residual impurities. Rinsing was continued until the external solution remained clear and colorless, signifying the thorough removal of unreacted thionine, as illustrated in Scheme 1. A subset of the final product was filtered and dried in a vacuum oven at 60 °C for 24 hours for physical characterization. The remaining amount was used immediately for electrode fabrication and electrochemical analysis to prevent aggregation of GONRs/Th.

2.4. Physical, chemical, and electrochemical characterization

Absorption spectra in the UV-visible range were obtained using a Model Cary UV-vis Agilent G51911AA spectrophotometer to explore the interaction between Th and GONRs. Crystallographic characteristics were examined using a powder X-ray diffractometer (XRD; Bruker D8 Advance) with a scan range of 10°–90° in 0.02° steps. Functional groups were identified by Fourier transform infrared spectroscopy (FT-IR; JASCO model 6300 type A) over the spectral range of 400–4000 cm^{-1}, using KBr as the reference. Surface composition analysis was performed with X-ray photoelectron spectroscopy (XPS; Thermo Scientific ESCALAB 250Xi, USA) using Al Kα radiation (15 kV, 600 W). Morphology was observed through field-emission scanning electron microscopy (FE-SEM, Hitachi, Tokyo) and transmission electron microscopy (JOEL JEM-2100Plus). Elemental composition was determined with an energy-dispersive X-ray spectrometer (EDX) attached to the SEM. Thermal behavior was studied using thermogravimetric analysis (TGA) with a TA Q50 instrument. All electrochemical tests are conducted using a potentiostat/galvanostat (Bio-Logic SP-300, France), operated with EC-Lab v11.61 software. In experiments employing a three-electrode configuration, a gold coil serves as the counter electrode. At the same time, $Hg/HgSO_4$/1.0 M H_2SO_4 (MSE, E_0 = 0.616 V *vs.* SHE) functions as the reference electrode, with potential values adjusted to the reversible hydrogen electrode (RHE). 1 M H_2SO_4 was selected as it exhibits high ionic conductivity, low internal resistance, high stability, and rapid proton transport, which support efficient charge transfer and provide a reliable means of assessing the material's intrinsic electrochemical performance for supercapacitors and the HER. Additionally, acidic electrolytes enhance pseudocapacitive behavior associated with surface redox-active sites and the HER catalytic activity of carbon-based materials, making them particularly useful for fundamental performance testing.[30,37]

2.5. Fabrication of electrodes/devices

The GONRs/Th electrodes were fabricated using a graphite sheet as the current collector and an aqueous 1.0 M H_2SO_4 electrolyte. An active material suspension with a Nafion binder (ratio of 9 : 1 by weight) was prepared in water by ultrasonication for 10 minutes to achieve uniform dispersion. This suspension was then sprayed onto the graphite sheet using an airbrush, covering an area of 1 cm^2 and yielding a mass loading of approximately 1 mg cm^{-2}, with only 90% of the mass attributable to the active material. For constructing a symmetric GONRs/Th//GONRs/Th device, cellulosic filter paper served as the separator, and all components were pressed between two acrylic sheets in an electrolyte containing 1.0 M H_2SO_4, as shown in Fig. S1.

2.6. Electrochemical studies for supercapacitors and hydrogen production

Electrochemical properties of the developed supercapacitor electrodes were examined using galvanostatic charge–discharge (GCD), cyclic voltammetry (CV), and electrochemical impedance spectroscopy (EIS). CV measurements were performed at scan rates of 2–100 mV s^{-1}, while GCD tests were conducted at current densities of 1–10 A g^{-1} to calculate the specific

capacitance (C_s). The C_s value (F g^{-1}) was obtained from the GCD data using eqn (1).

$$C_s = I\Delta t/(m\Delta V) \quad (1)$$

I (A) indicates the current applied, ΔV(v) represents the potential window, Δt (s) indicates the discharge duration, and the mass of the active substance is represented by m (g).

The calculations for energy density E (Wh kg^{-1}) and power density P (W kg^{-1}) are performed using eqn (2) and (3), respectively:

$$E = \frac{1}{7.2}C_s(\Delta V)^2 \quad (2)$$

$$P = E/\Delta t(h) \quad (3)$$

Eqn (4) and (5) were employed to determine the respective contributions of surface and diffusion currents in profiling the I(v) as follows:

$$I_V = K_1 v + K_2 v^{0.5} \quad (4)$$

$$I_V/v^{0.5} = K_1 v^{0.5} + K_2 \quad (5)$$

The potential-dependent current, denoted as I(V), was obtained from cyclic voltammetry measurements performed at various scan rates. The scan rate, denoted as v, was expressed in mV s^{-1}. Constants K_1 and K_2 were determined by plotting the normalized current against the scan rate, specifically by graphing $I_V/v^{0.5}$ *versus* $v^{0.5}$, and extracting the slope and intercept. These constants, $K_1 v$ and $K_2 v^{0.5}$, correspond to the current components controlled by surface redox processes and diffusion, respectively. Electrochemical impedance spectroscopy was conducted at the open-circuit potential, using a 5 mV excitation amplitude over the frequency range of 0.1 Hz–100 kHz. The resulting data were processed using EC-Lab software.

To evaluate the electrocatalytic activity of the fabricated electrodes for the hydrogen evolution reaction (HER), the electrodes were first conditioned through electrochemical cycling, consisting of 50 voltammetry sweeps at a scan rate of 100 mV s^{-1} within a potential window of −0.9 to −0.5 V *versus* MSE (corresponding to −0.284 to 0.116 V *versus* RHE). This was followed by linear-sweep voltammetry at 10 mV s^{-1}, starting at 0.5 V *vs.* MSE (0.116 V *vs.* RHE) until the current density reached 100 mA cm^{-2}. Electrochemical impedance spectroscopy was performed at −0.78 V *vs.* MSE (−0.164 V *vs.* RHE) with a 5 mV AC perturbation, spanning 0.1 Hz to 100 kHz. All measurements were performed under ambient conditions, with adjustments made to account for IR drops.

3. Results and discussion

3.1. Chemical and physical characterization

EDS analysis was conducted to confirm the synthesis of GONRs/Th composites at RT and HT and to identify compositional differences. For pristine GONRs, only carbon (C) and oxygen (O) were detected (Table 1), consistent with their expected composition. In contrast, both GONRs/Th (RT) and GONRs/Th (HT) exhibited additional sulfur (S) and nitrogen (N), confirming the incorporation of thionine. Notably, the HT composite contained higher C and S and lower O compared to the RT sample, suggesting greater thionine insertion. These results validate the formation of composites and underscore the effect of synthesis conditions on the chemical composition.

Table 1 EDS results of GONRs, GONRs/Th (RT), and GONRs/Th (HT) samples

Material	C atomic%	O atomic%	N atomic%	S atomic%
GONRs	86.4	13.6	—	—
GONRs/Th (RT)	43.5	35.8	19.8	0.9
GONRs/Th (HT)	53.1	30.5	13.5	2.9

SEM and TEM were used to characterize the shape and structure of GONRs/Th (RT) and GONRs/Th (HT) and to identify differences arising from the two synthesis methods. As illustrated in Fig. 1a, original GONRs display a layered, sheet-like appearance with visible wrinkles and stacking features. Such stacking is common in graphene-based materials and can restrict the available surface area for electrolyte contact, thus influencing electrochemical performance. In the case of GONRs/Th (RT) and GONRs/Th (HT) composites, the SEM images illustrated in (Fig. 1b) and (Fig. 1c) reveal the retention of the sheet-like structure of GONRs, with slight sheet separation between nanoribbons, resulting from thionine intercalation. The SEM image of GONRs/Th (HT) (Fig. 1c) shows a more compact structure, likely due to temperature-dependent intercalation mechanisms. At RT, thionine molecules may bind to GONRs differently than at HT, which is expected to influence both the supercapacitive and electrocatalytic behavior of the composites.

To verify that MWCNTs were properly unwrapped into nanoribbons, Fig. 1d displays the lamellar layers of GONRs. TEM imaging of the composites further confirmed the insertion of thionine. For GONRs/Th (RT) (Fig. 1e), few-layered GONRs with evident interlayer spacing and wrinkling indicate successful thionine intercalation, which prevented restacking. In contrast, GONRs/Th (HT) (Fig. 1f) displays a compact structure with little to no spacing, suggesting that hydrothermal conditions promote a different interaction between GONRs and thionine. The absence of a clear interlayer separation indicates stronger interaction between the GONRs and thionine than in the RT sample. These findings highlight the role of synthesis conditions in determining the material's architecture and, consequently, its electrochemical behavior.

To investigate the structural and electronic properties of the prepared materials and confirm the integration of thionine into GONRs, multiple spectroscopic techniques were employed. X-ray diffraction (XRD) analysis was performed to analyze the crystal structure, as shown in Fig. 2a. The unmodified GONRs exhibit three distinct diffraction peaks at a 2θ angle of 24.7°, associated with the (002) plane, with a full width at half maximum (FWHM) of 6.1. This pattern is characteristic of graphitic materials, indicating the spacing between graphene

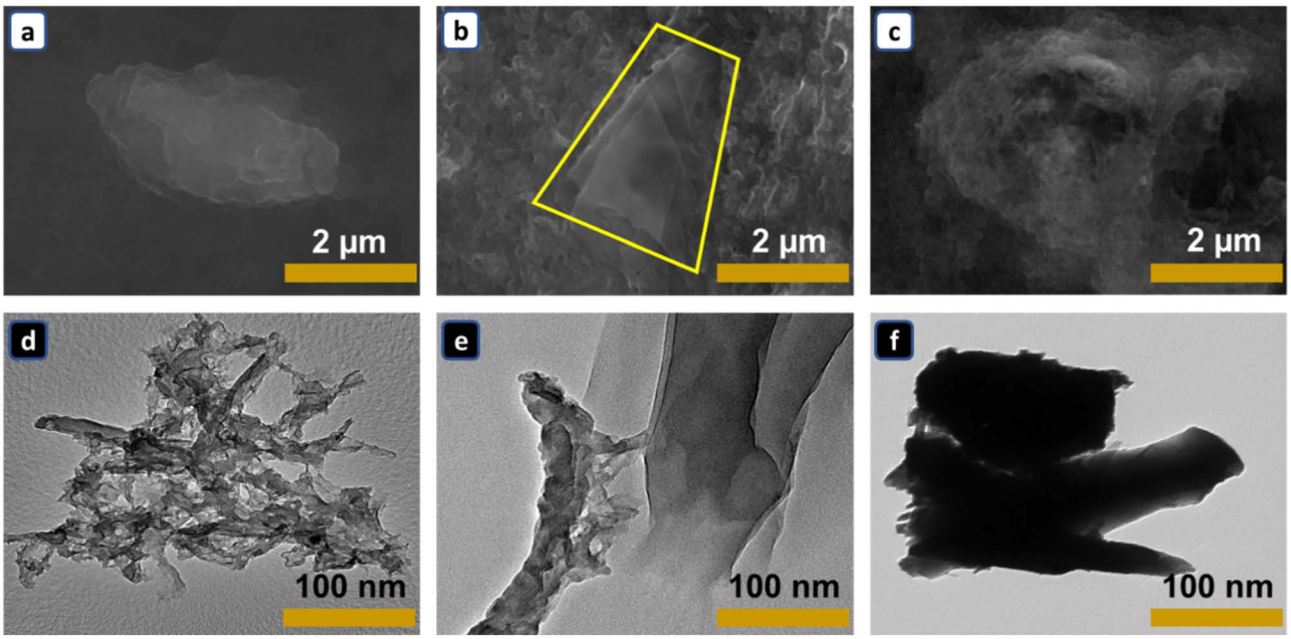

Fig. 1 The SEM and TEM of (a and d) GONRs, (b and e) GONRs/Th (RT), and (c and f) GONRs/Th (HT).

sheets is influenced by oxygen-containing groups. Additional peaks at 43° (linked to the (100) plane) and 78.5° (related to the (006) plane) indicate the effective unzipping of multi-walled carbon nanotubes (MWCNTs) and the formation of GONRs, consistent with previous observations in similar structures.[30,38–40]

Upon thionine incorporation, the XRD patterns of GONRs/Th composites exhibit a notable shift in the (002) peak position to 26.1° and 25.9° and a significant decrease in the FWHM (sharper peaks) to 3.4 and 3.2 for GONRs/Th (RT) and GONRs/Th (HT), respectively. In addition, the relative intensity of the peaks at 43° (100) and 78.5° (006) significantly reduced. These structural changes suggest that thionine intercalation promotes improved graphene sheet alignment and partially restores graphitic order. Such changes are attributed to π–π interactions between thionine molecules and GONRs and the bond formation between thionine and the oxygen-based functional groups of the GONRs, which forces the ordering of the GONRs.[41,42]

UV-vis absorption spectroscopy was employed to investigate the electronic interactions and verify the grafting of thionine onto GONRs (Fig. 2b). Pristine GONRs exhibit a characteristic absorption band at 260 nm, assigned to the π → π* transition

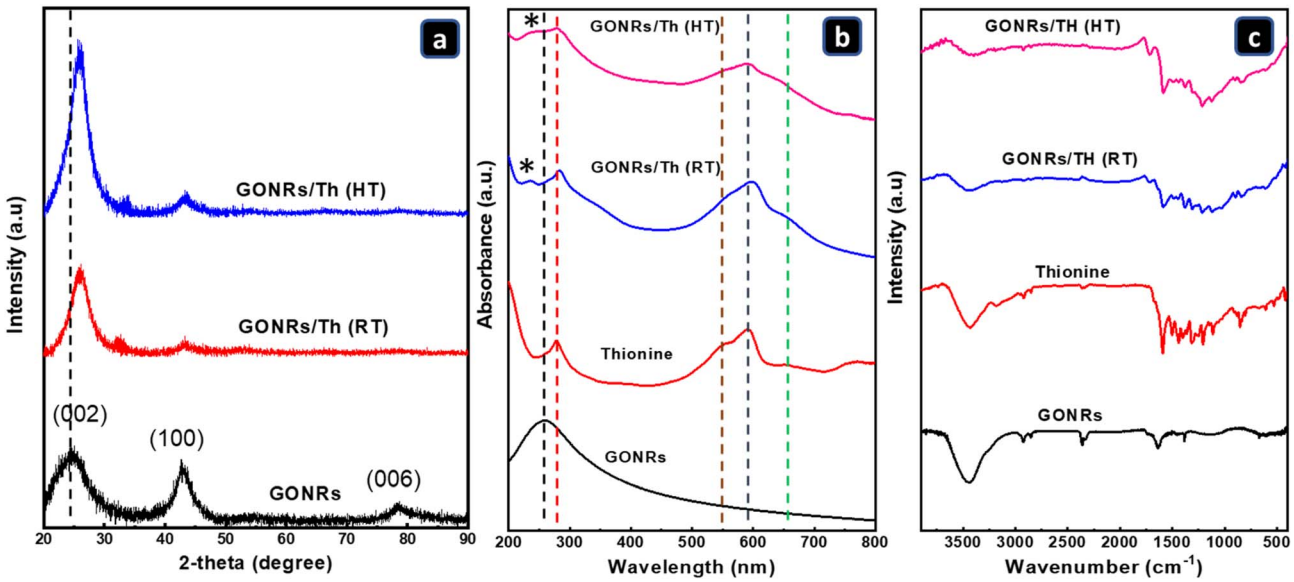

Fig. 2 (a) XRD patterns, (b) UV-vis absorption spectra, and (c) FT-IR spectra of GONRs, Th, GONRs/Th (RT), and GONRs/Th (HT).

of aromatic C=C bonds,[41] with negligible absorbance between 550–650 nm. In contrast, thionine shows two bands at 278 nm, corresponding to the $\pi \rightarrow \pi^*$ transition of the aryl rings, and 592 nm, corresponding to the $n \rightarrow \pi^*$ transition of C=N bonds, along with a shoulder at 550 nm from T-type dimer aggregates.[43]

For the GONRs/Th composites (RT and HT), all thionine peaks were observed, with a slight shift of the GONR band to shorter wavelengths, confirming successful grafting and strong interactions between GONRs and thionine. The composites also showed enhanced absorbance at 655 nm compared to pristine thionine, more pronounced in the GONRs/Th (HT) composite, attributed to strong π–π interactions, improved electronic coupling, and, hence, charge transfer between the thionine conjugated system and the GONR sheets.[44] Furthermore, a notable increase in the intensity of the dimer band at 550 nm relative to the monomer peak at 592–597 nm, particularly in the HT composite, suggests stronger π–π interactions under hydrothermal conditions and that thionine shifts towards the dimeric form when adsorbed onto GONRs.[45] Additionally, a slight redshift (~5 nm, from 592 to 597) in the RT composite reflects enhanced delocalization of π-electrons across the conjugated GONRs/Th framework. Collectively, these results confirm that covalent amide bonding, electrostatic forces, π–π stacking, and electronic coupling synergistically stabilize the composites and govern their electronic communication.

The FT-IR spectra of the samples are shown in Fig. 2c. A broad absorption band at 3440 cm^{-1} is observed in all samples, corresponding to O–H stretching vibrations from hydroxyl groups in GONRs and adsorbed moisture. For the unmodified GONRs, peaks at 2930 and 2860 cm^{-1} are linked to ν(C–H) stretching in CH2 and CH_3 groups. Additionally, signals at 2360 and 2340 cm^{-1} are indicative of ν(O–C=O), suggesting the presence of carbon dioxide or carboxylate functionalities.[46] A prominent feature at 1639 cm^{-1} is associated with δ(O–H) bending in C–OH groups and/or stretching vibrations of C–O or C–O–C bonds, indicating the presence of oxygen-related functional groups characteristic of oxidized graphene.[36,44]

The spectrum of free thionine shows characteristic bands, including C–S bending at 902 cm^{-1},[47] C–N stretching of the aromatic amines at 1320 cm^{-1},[48] N–H bending at 1604 cm^{-1}, and broad N–H stretching between 2930–3200 cm^{-1}, along with skeletal vibrations of the thionine aromatic rings at 1480 and 1388 cm^{-1}.[49] In the case of GONRs/Th composites, additional thionine fingerprint bands were observed compared to the pristine GONRs, confirming successful incorporation of thionine within the GONR structure. A slight shift in the bands is also observed, likely due to the π-network interactions between thionine and GONRs. Furthermore, the appearance of a C–N amide band at 1260 cm^{-1} suggests partial covalent conjugation.[50] At the same time, the peak at 1712 cm^{-1}, characteristic of C=O, shows a higher intensity in GONRs/Th (HT) than in GONRs/Th (RT). This finding, along with the identifiable peaks of thionine, indicates that thionine mainly interacts with GONRs through noncovalent π–π stacking. Nonetheless, there may also be some covalent bonding involved, especially in the HT sample, due to the more intense reaction conditions.[51]

TGA analysis was conducted to evaluate the thermal stability of unmodified GONRs and GONRs/Th composites fabricated at room temperature and at high temperature (Fig. S2). Pristine GONRs show two significant weight-loss steps at 30–100 °C, due to removal of adsorbed water, and 100–250 °C, from decomposition of oxygen-containing groups (carboxyl, hydroxyl, and epoxy),[52] characteristic of graphene oxide. In contrast, both GONRs/Th (RT) and (HT) composites exhibit reduced mass loss in the 100–250 °C range, indicating lower oxygen-functional group content and improved thermal stability. The RT composite shows a gradual weight loss between 250–300 °C, attributed to decomposition of thionine adsorbed on GONRs, confirming its successful incorporation. The HT composite exhibits less weight loss in this region, suggesting stronger interactions between thionine and the GONR matrix, resulting in greater thermal robustness.

These findings demonstrate that hydrothermal treatment enhances the stability of thionine–GONR interactions, underscoring the role of the synthesis method in dictating the composite's thermal behavior.

TGA analysis was conducted to assess the thermal stability and decomposition characteristics of the GONRs and the GONRs/Th hybrid composite samples prepared at room temperature and through a hydrothermal approach. The resulting TGA curves in Fig. S2 illustrate weight changes as temperature increases, providing information on functional groups and thermal stability. The pristine GONRs typically exhibit significant weight loss in two main stages. The initial weight loss observed between 30 °C and 100 °C is primarily attributed to the removal of adsorbed water molecules from the hydrophilic surface of graphene oxide (thermal behavior and thermolysis mechanisms of graphene oxide). A more substantial weight loss occurs between 100 °C and 250 °C, which corresponds to the elimination of labile oxygen-containing functional groups (*e.g.*, carboxyl, hydroxyl, and epoxy groups) present in the GONR structure.[52] This decomposition process is a characteristic feature of graphene oxide materials. In comparison to pristine GONRs, both the GONRs/Th (RT) and GONRs/Th (HT) hybrid composite samples demonstrate a lower content of oxygen-containing groups. This is evidenced by the reduced mass loss in the 100–250 °C range, suggesting an efficient removal of these oxygen functional groups during both the physical adsorption (RT) and hydrothermal processing (HT) reactions. Consequently, the GONRs/Th (RT) and (HT) composites exhibit no significant mass loss between 150 °C and 250 °C, indicating enhanced thermal stability in this temperature range due to reduced oxygen-containing functionalities. Furthermore, as illustrated in Fig. S2, the GONRs/Th (RT) sample displays a gradual weight loss from approximately 250 °C to 300 °C. This specific weight loss can be attributed to the slow decomposition of thionine molecules weakly attached to the surface of the GONRs. This observation confirms the successful incorporation of thionine and indicates its thermal stability within the composite. Conversely, for GONRs/Th (HT), the sample exhibited less significant mass loss in this temperature range, indicating greater thermal stability and less decomposition of

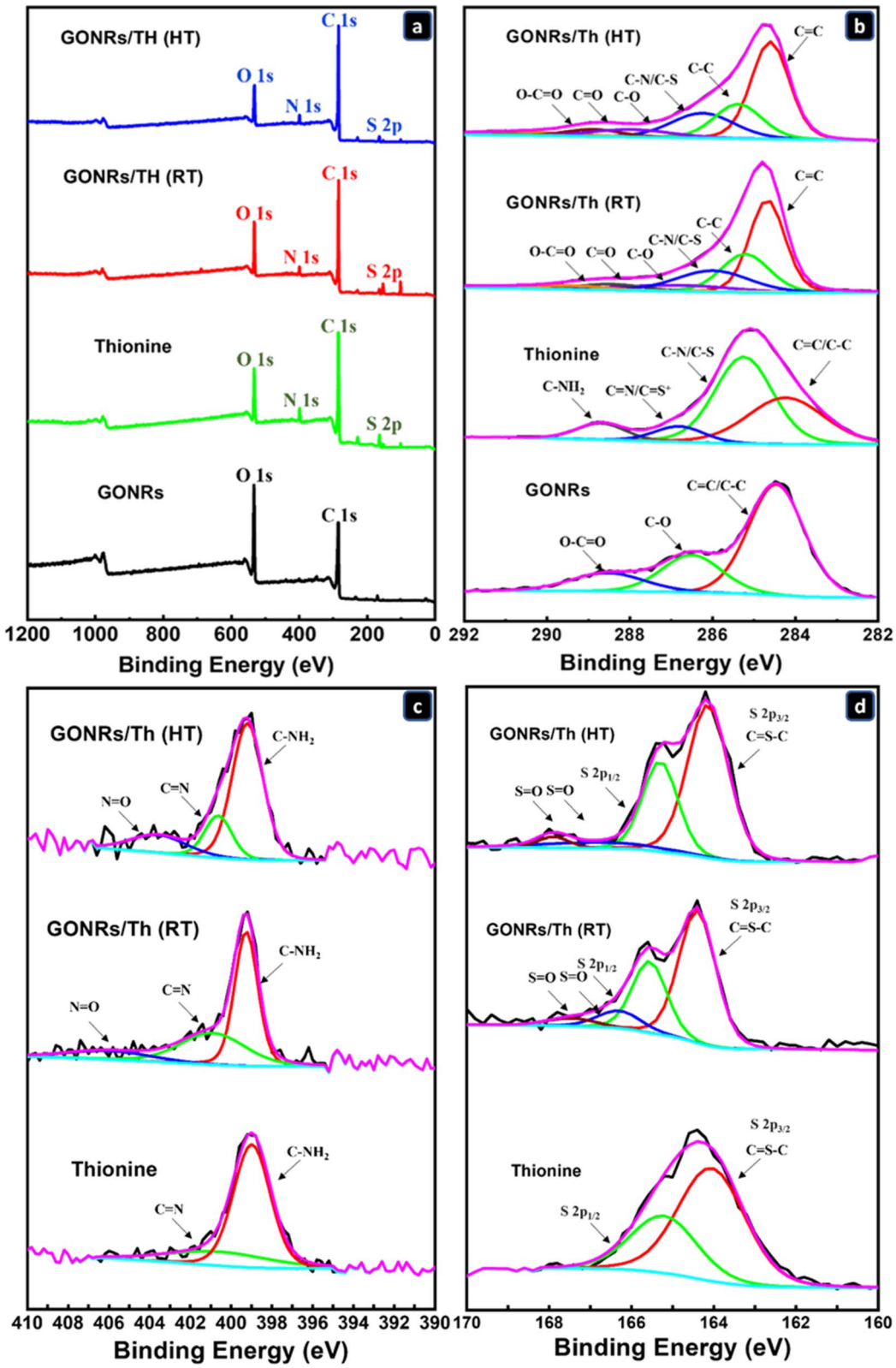

Fig. 3 XPS of GONRs, Th, GONRs/Th (RT), and GONRs/Th (HT): (a) fast survey scan mode, (b) C 1s, (c) N 1s, and (d) S 2p.

the thionine component. This suggests that hydrothermal treatment leads to a more stable interaction of thionine with the GONR matrix, making the materials more thermally robust. The enhanced stability of the HT composite highlights the influence of the preparation method on the overall integrity of the thionine-GONR interaction.

Table 2 XPS weight percentage peak area from the elemental analyses for GONRs, thionine, GONRs/Th (RT), and GONRs/Th (HT) samples

Materials	C 1s at. %	O 1s at. %	N 1 s at. %	S 2p at. %
GONRs	69.78	29.27	—	—
Thionine	76.30	12.36	4.23	4.72
GONRs/Th (RT)	71.85	13.88	2.95	2.07
GONRs/Th (HT)	80.95	12.57	2.83	2.94

Raman spectroscopy, a non-destructive tool for probing carbon-based materials, provides valuable insight into the structural properties of GONRs and their thionine composites (Fig. S3).[53] The key spectral features are the G band ($\sim$1580 cm^{-1}), arising from sp^2 carbon vibrations, and the D band ($\sim$1350 cm^{-1}), associated with defects, disorder, and edge effects. The intensity ratio (I_D/I_G) is a measure of defect density, with higher values indicating greater disorder.[54] Pristine GONRs exhibit an I_D/I_G ratio of 0.85, reflecting significant defects generated during CNT unzipping and oxidation.[55] For the GONRs/Th (RT) composite, this ratio increases to 0.93, suggesting that thionine adsorption introduces additional disorder, likely by disrupting the sp^2 network or forming new bonds.[56] Thionine itself shows distinct Raman features, including a strong band near 1600 cm^{-1} (C=N stretching), along with aromatic ring and N–H vibrations,[57] which contribute to the broad bands observed in the RT composite. In contrast, the GONRs/Th (HT) composite exhibits an I_D/I_G ratio of 0.84, nearly identical to that of pristine GONRs and markedly lower than that of the RT sample. This indicates that hydrothermal treatment partially restores graphitic ordering, likely by removing oxygen functional groups and aligning thionine more closely on the GONR's surface.[58] These findings highlight the substantial influence of synthesis temperature on structural ordering and defect density.

X-ray photoelectron spectroscopy (XPS) was employed to determine the chemical composition of the samples. The overall spectra in Fig. 3a revealed peaks corresponding to carbon 1s and oxygen 1s in all samples, with the GONRs/Th (RT) and GONRs/Th (HT) composites showing increased carbon levels and reduced oxygen compared to unmodified GONRs. As summarized in Table 2, this trend corroborates the XRD and EDS results, confirming the reduction of oxygen functionalities after treatment. In addition, nitrogen and sulfur signals were detected in both composites, with their contents roughly half that of thionine, evidencing effective functionalization. The deconvoluted C 1s, N 1s, and S 2p spectra are presented in Fig. 3b–d.

The deconvoluted C 1s spectrum of pristine GONRs (Fig. 3b) displayed a C=C/C–C peak at 284.46 eV, along with signals at 286.5 eV and 288.53 eV corresponding to C–O–C/C–O and O–C=O groups, respectively. These features align with common findings in studies of graphene oxide, where oxygen-containing groups are typically found on basal planes and edges.[59] Thionine exhibited four peaks, corresponding to C=C/C–C (284.46 eV), C–N/C–S (285.5 eV), C=N/C=S^+ (287.22 eV), and C–NH_2 (289.37 eV). Following RT and HT treatments, oxygen-related peaks decreased markedly, indicating a reduction of GONRs and bond formation with thionine. The persistence of the C=C peak and appearance of a shakeup satellite near 290 eV confirmed retention of the conjugated graphene structure, consistent with the EDS results.[60]

The N 1s spectrum of thionine (Fig. 3c) displayed peaks at 399 eV (C–NH_2) and 401 eV (C=N–).[61] These features remained in the composites, confirming structural preservation of thionine. In GONRs/Th (HT), however, an additional peak at 401–403 eV was observed, attributed to C–NH–C=O bonds,[62,63] suggesting covalent interactions between thionine amines and GONRs under hydrothermal conditions.

The S 2p spectrum in Fig. 3d revealed a characteristic spin–orbit doublet (S $2p_{3/2}$ and S $2p_{1/2}$, $\Delta \approx 1.16$ eV). In pure thionine, a single peak was observed, deconvoluted into S $2p_{3/2}$ and S $2p_{1/2}$ peaks at $\sim$164 and 165.2 eV, corresponding to heterocyclic C=S–C bonds of the phenothiazine core.[64,65] In the composites, these peaks shifted slightly, reflecting interactions with GONRs, and additional peaks emerged at 166–167 eV, characteristic of oxidized sulfur species (S=O and SO_3^{2-}).[66] These features indicate that oxygen groups on GONRs react with the sulfur-containing moieties of thionine during synthesis. Collectively, the XPS results confirm successful functionalization of GONRs with thionine, involving both noncovalent π–π stacking and covalent interactions.

4. Electrochemical evaluation

To evaluate the surface area of the synthesized materials under conditions like the intended application, electrochemical surface area (ECSA) analysis was performed, and the results are shown in Fig. S4. ECSA values of 191.5, 198.3, and 193 $m^2\ g^{-1}$ are obtained for GONRs, GONRs/Th (RT), and GONRs/Th (HT), respectively, indicating a similar surface area arising mainly from the GONRs, with an insignificant increase in the presence of thionine. Nitrogen adsorption–desorption (BET) measurements often underestimate or misrepresent the electrochemically accessible surface area of 2D carbon-based materials because of the highly stacked, compact structure of GONRs in powder form; therefore, this method was not employed in this study. By contrast, during the ECSA measurements, the film was fabricated by spraying the as-synthesized suspension and was allowed to swell slightly in aqueous media.

4.1. Supercapacitor study

Electrochemical analysis was performed to investigate the capacitance characteristics of GONRs and GONRs/Th (RT) and GONRs/Th (HT) composites to understand the dynamics and process of charge accumulation in the electrode reactions and to identify the ideal potential range that avoids unwanted electrochemical side reactions. The CV curves of GONRs, GONRs/Th (RT), and GONRs/Th (HT) at scan rates of 2 to 100 mV s^{-1} in 1 M H_2SO_4 are shown in Fig. S5a–S5c, respectively. For comparison, Fig. 4a shows the curves of CV at a fixed

scan rate (20 mV s^{-1}). The CV curves of GONRs exhibited clear redox peaks associated with oxygen-containing functional groups present in the material. Upon incorporation of thionine, as confirmed by XPS and FT-IR analyses, the GONRs/Th composites exhibited enhanced redox activity, showing markedly higher current densities in both anodic and cathodic directions compared to pristine GONRs and enhanced capacitive performance, as reflected by the increase in double-layer current at 0.4 V *vs.* MSE. The improved pseudocapacitive behavior of GONRs/Th under acidic conditions, attributed to the amino groups present in thionine molecules, highlights the suitability of thionine for enhancing redox supercapacitance contribution.[67,68] However, the preparation method influences both capacitance and potential window. As shown in Fig. 4a, the composite synthesized *via* the RT method delivers higher capacitance and a broader potential window than the HT-prepared counterpart, offering a distinct advantage for supercapacitor applications. Furthermore, because all GONR-based materials exhibited similar ECSA (Fig. S4), enhanced capacitance should be attributed to intrinsic redox-active sites and their pseudocapacitance contribution rather than to high surface area or porosity.

These findings highlight the dual role of thionine incorporation within the GONR framework. First, it slightly enhances the double-layer capacitance contribution by expanding the interlayer spacing of GONRs, thereby exposing the electrolyte to a larger active surface area, but primarily causes a significant increase in pseudocapacitance due to the fixation of thionine at the GONR surface. Second, the GONR framework inhibits thionine agglomeration, enhances electrical conductivity, enables faster and more extensive redox reactions, and strengthens GONR–thionine interactions, as confirmed by FTIR and XPS analyses. Consequently, this synergistic effect results in higher capacitance, greater charge-storage capacity, and improved conductivity.

To analyze the kinetics of interactions between electrodes and electrolytes at various charging and discharging speeds, a current profile diagram was developed utilizing eqn (4) and (5), as shown in Fig. 4b. This analysis distinguishes between the surface contributions of controlled (non-diffusion-limited) and bulk-controlled (diffusion-limited) EDLC currents at different scan rates at a specific potential (0.2 V *versus* MSE). At lower scan rates, the bulk contribution ranged from 62% to 70% of the total current across all examined materials, but this proportion decreased markedly to 18–25% at 100 mV s^{-1}. These findings suggest that at slower scan rates, ions have ample time to reach interlayer regions. In contrast, at higher scan rates, ion intrusion into these areas is hindered, limiting whole charge storage. Notably, the surface-EDLC contribution of GONRs/Th (RT) was the highest at all scan rates, underscoring the effectiveness of the RT method for integrating thionine with GONRs. This approach provides adequate interlayer spacing, enabling deeper electrolyte penetration into the GONR framework, as confirmed by TEM and SEM, thereby enhancing the composite's overall capacitance.

The overall capacitance contribution from bulk and surface EDLCs can be more accurately assessed by applying the power law detailed in eqn (6) to the CV curves of the prepared electrodes.,[69]

$$\log I(\mathrm{v}) = a + b \log(\nu) \quad (6)$$

The statement indicates that I represents the current at a specific potential and scan rate (ν), with parameters a and b serving as adjustable factors. In this context, b corresponds to the slope, while a denotes the intercept of the line. The value of b provides essential insights into the charge-storage mechanism: a b value close to 0.5 suggests a process dominated by diffusion, whereas a value near 1 implies a surface-controlled process, associated with higher power capability.[70] The power-law relationship between log current and log scan rate is illustrated in Fig. 4c, using anodic current values at 0.2 V *vs.* MSE for different scan rates. The similarly calculated b values (0.79–0.81) for GONRs, GONRs/Th (HT), and GONRs/Th (RT) suggest comparable capacitive charge-transfer behavior across the samples. Nevertheless, the total capacitance of the GONRs/Th composites greatly exceeds that of GONRs alone, as indicated by the consistent positive shift in log I across all scan rates, with GONRs/Th (RT) exhibiting the highest capacitance. This demonstrates enhanced ion transport at the electrode–electrolyte interface and throughout the electrode material, thereby increasing charge storage capacity.

The electrochemical characteristics of the prepared materials were assessed using galvanostatic charge/discharge (GCD) measurements to evaluate their specific capacitance (C_s) at various charge and discharge rates. The GCD profiles at different current densities (1–10 A g^{-1}) are presented in Fig. S5d–S5f for GONRs, GONRs/Th (RT), and GONRs/Th (HT), respectively. For comparison, the GCD curves at 1 A g^{-1} for these materials are shown in Fig. 4d. All samples display a quasi-triangular charge/discharge pattern, indicative of good electrical conductivity, low IR drop, and efficient charge transfer. The apparent difference in the potential limits during GCD measurements results from variations in the operating potential window among the materials studied, since the potential range was individually adjusted for each electrode to retain high coulombic efficiency and ensure stable electrochemical operation. GONRs/Th (RT) demonstrated superior capacitance at a 1 A g^{-1} charging/discharging current of 732 F g^{-1}, compared to GONRs (501 F g^{-1}), indicating the significant impact of incorporating and drafting thionine within the GONR layer. GONRs/Th (HT) exhibited a slightly lower capacitance of 635 F g^{-1}, attributed to the preparation method, which affects the extent and structure of thionine insertion/grafting and, consequently, the rate of charge transport, resulting in decreased pseudocapacitance.

Fig. 4e compares the specific capacitance (C_s) of the studied materials at different charge/discharge current densities (1–10 A g^{-1}). As the current density increases, the C_s values decrease because ions are less able to penetrate deeply into the electrode bulk. Nevertheless, at the highest current density, all substances retained elevated C_s, indicating their outstanding performance. The comparative results across different current densities clearly demonstrate a substantial enhancement in the

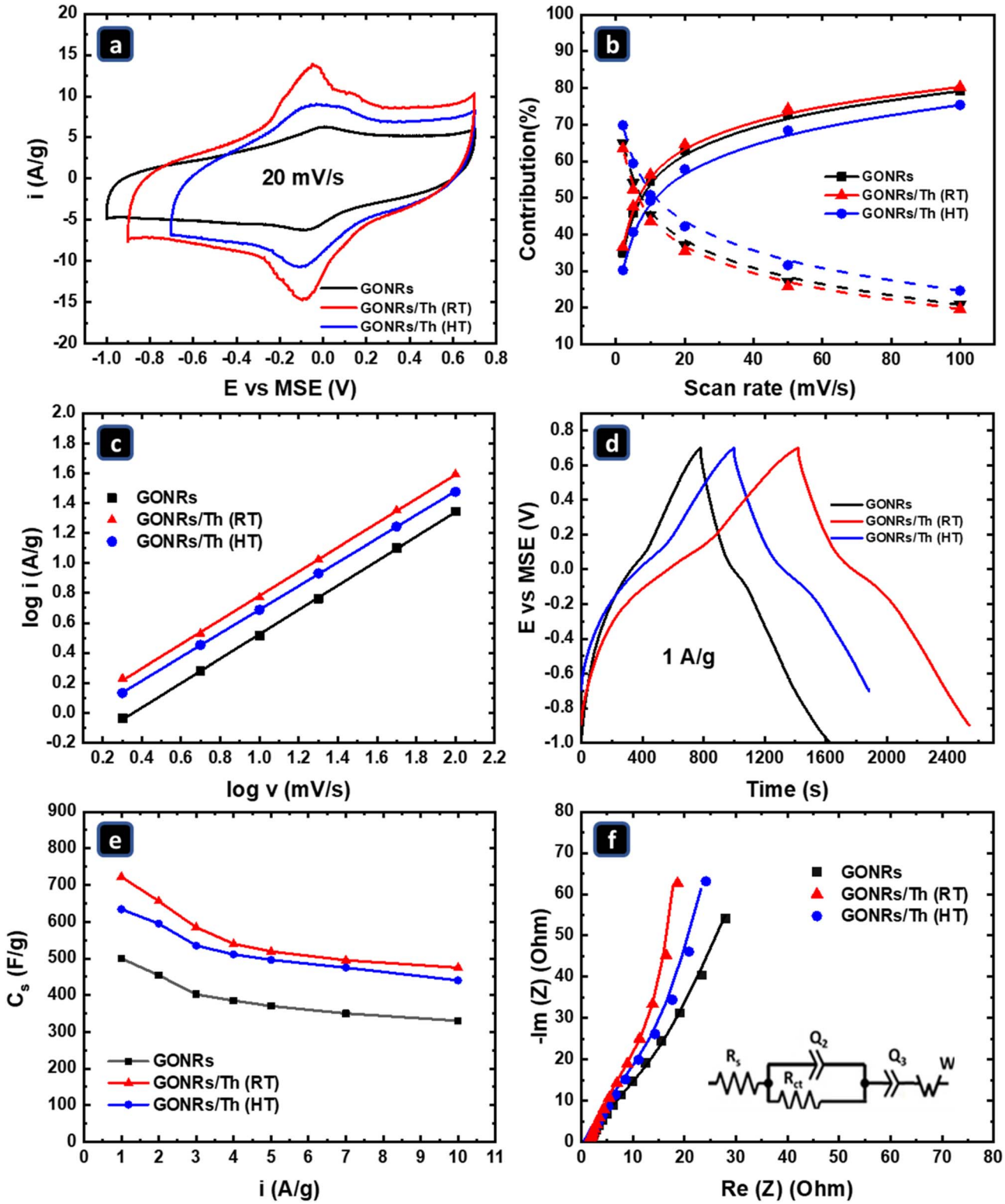

Fig. 4 (a) Cyclic voltammetry profiles recorded at a scan rate of 20 mV s^{-1}, (b) the percentage contributions of diffusion-controlled (dashed line) and non-diffusion-controlled currents (solid line) at 0.2 V *versus* MSE across various scan rates, (c) the relationship between the log *I* and the log scan rate at 0.2 V *versus* $Hg/HgSO_4$, (d) galvanic charge–discharge curves at a current density of 1 A g^{-1}, (e) specific capacitance values at current densities ranging from 1 to 10 A g^{-1}, and (f) EIS plots at open circuit potential, with the equivalent circuit model shown in the inset.

Table 3 Comparison of the specific capacitance exhibited by thionine/carbon composite materials and various related categories

Electrodes	Electrolytes	Specifications	C_s (F g^{-1})	References
rGO/PANI	1 M H_2SO_4	0.5 A g^{-1}	261	72
Th-GA[a]	1 M H_2SO_4	1 A g^{-1}	512	67
rGO-HGB[b]	1 M H_2SO_4	1 A g^{-1}	221	73
GO/NC[c]	6 M KOH	1 A g^{-1}	405	74
Graphdiyne nanostructures	1M Na_2SO_4	3.5 A g^{-1}	71	75
Pea protein-derived carbons	1M KOH	1 A g^{-1}	413	76
N-doped ordered mesoporous carbon/ graphene	2M KOH	1 A g^{-1}	2.46	77
N-doped graphene sheets	1 MH_2SO_4	1 A g^{-1}	242	78
Th-GONRs	1 M H_2SO_4	1 A g^{-1}	732	Current work

[a] Thionine functionalized 3D graphene aerogel. [b] Benzenediols@hydrogel rGO. [c] Graphene oxide/polybenzoxazine/porous carbon.

capacitive behavior of GONRs when they are composed with thionine *via* the RT method. Additionally, the rapid mobility and compact size of H^+ ions in H2SO4 enhance ion transfer, thereby increasing capacitance across all examined materials.[71] Table 3 presents the capacitive performance of similar materials prepared by different synthesis methods and compares them with those prepared in this study.

EIS was employed to investigate the electrochemical characteristic of the synthesized materials, with results illustrated in Fig. 4f. The inset of this figure displays the equivalent circuit model used to interpret the data. The circuit features include R_s (the electrolyte and contact series resistance), R_{ct} (the resistance to charge transfer), Q_2 and Q_3 (representing pseudocapacitance and electric double-layer capacitance as constant-phase elements), and W (the Warburg impedance),[79–81] with the different fitting values reported in Table 4.

Fig. 4f displays a faint semicircular feature at high frequencies, as obtained from fitting the data, indicating a low charge-transfer resistance (R_{ct}) at the electrodes. The R_{ct} values show minimal differences across samples (Table 4), supporting the presence of rapid redox processes facilitated by nitrogen- and oxygen-containing functional groups.

Two distinct linear regions with different slopes are observed in the Nyquist plots, reflecting diffusion-limited behavior governed by the electrode's structure and composition. At high to medium frequencies, the response is dominated by ion transport to easily accessible surface sites due to the limited time available for diffusion. In contrast, at low frequencies, ions penetrate deeper into the bulk, reaching interlayer regions within the GONR framework as sufficient diffusion time becomes available. The GONRs/Th (RT) electrode shows the most pronounced slopes in both regimes, suggesting minimal ion-diffusion resistance and enhanced capacitive performance (Fig. 4f). The Warburg diffusion resistance (W) follows the order GONRs/Th (RT) < GONRs/Th (HT) < GONRs (Table 4), further validating the enhanced ion-transport efficiency of the RT-prepared composite.

Moreover, the combined $Q_2 + Q_3$ (PC + EDLC) values follow the same trend: GONRs/Th (RT) > GONRs/Th (HT) > GONRs. The pronounced increase in $Q_2 + Q_3$ for GONRs/Th (RT) highlights superior electrolyte accessibility and more efficient ion diffusion within the electrode matrix, key attributes for improved energy storage performance. Additionally, the higher $Q_2 : Q_3$ ratio for GONRs/Th (RT) compared to the other samples indicates a greater pseudocapacitive contribution, underscoring the synergistic effect of GONRs and thionine in enhancing charge-storage capability.

To assess the electrochemical performance of the GONRs/Th composites as supercapacitor electrodes, GONRs/Th(RT)// GONRs/Th(RT) and GONRs/Th (HT)//GONRs/Th (HT) symmetrical two-electrode configurations were constructed. Cyclic voltammetry measurements at scan rates from 2 to 100 mV s^{-1} are shown in Fig. S6a and S6b. Both arrangements exhibited stable operation over a potential span of up to 1.7 V, showing no faradaic signals from hydrogen or oxygen evolution, indicating their potential for high-voltage aqueous supercapacitors. Fig. 5a compares CV curves at 20 mV s^{-1} for both setups, highlighting the enhanced electrochemical response of the GONRs/Th (RT)// GONRs/Th (RT) configuration. The broader CV area and more rectangular shape indicate enhanced capacitive behavior and improved charge-transport kinetics. These observations highlight the excellent voltage tolerance and efficient redox activity of the GONRs/Th composites, particularly for the RT-prepared electrodes.

Table 4 The values of the EIS data fitting for GONRs, GONRs/Th (HT), and GONRs/Th (RT)

Electrode material	R_{ct} (PC) (Ohm)	Q_2 (PC) (F $s^{(a-1)}$)	($^a a_2$)	Q_3 (EDLC) (F $s^{(a-1)}$)	($^a a_3$)	W (Ohm $s^{-1/2}$)
GONRs	6.7 ± 0.8	0.32 ± 0.09	0.92	0.21 ± 0.05	0.83	2.8 ± 0.2
GONRs/Th (RT)	5.6 ± 0.7	0.56 ± 0.05	0.98	0.35 ± 0.001	0.92	1.7 ± 0.1
GONRs/Th (HT)	6.2 ± 0.4	0.45 ± 0.01	0.97	0.29 ± 0.004	0.87	2.08 ± 0.06

[a] The ideality factor (a) indicates the degree to which Q behaves ideally.

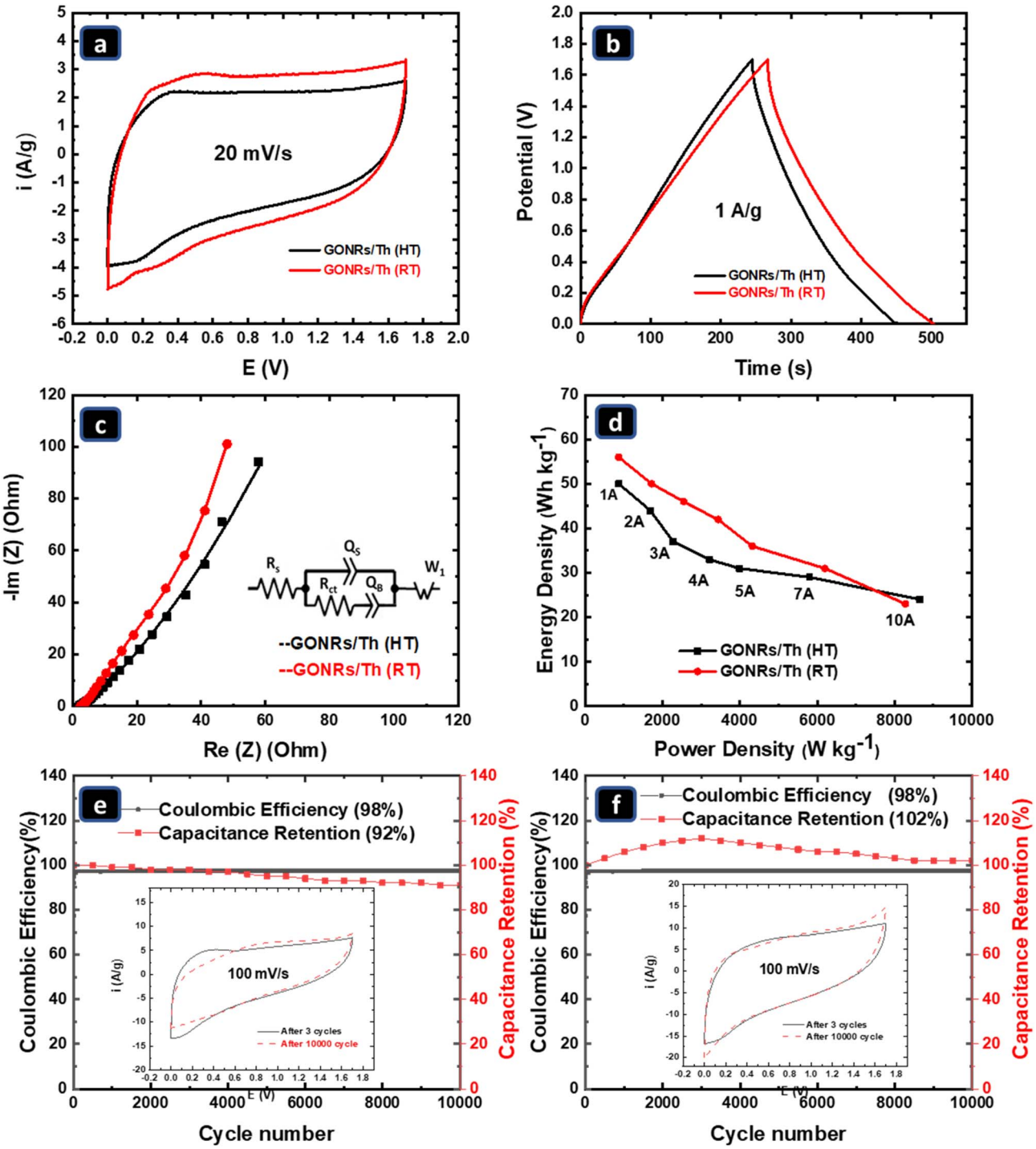

Fig. 5 (a) Cyclic voltammetry profiles recorded at a 20 mV s^{-1} scan rate, (b) galvanostatic charge–discharge responses at a current density of 1 A g^{-1}, (c) Nyquist plots derived at OCP, including the fitted equivalent circuit (inset), (d) Ragone plots at various current densities, and (e and f) data on cycling performance and capacitance retention at 10 A g^{-1} over 10 000 charge–discharge cycles in 1 M H_2SO_4. Inset images show CV curves at 100 mV s^{-1} after 3 and 10 000 cycles for symmetric devices with GONRs/Th (RT) and GONRs/Th (HT) configurations.

Fig. 5b presents the galvanostatic charge–discharge profiles of the symmetric devices at a current density of 1 A g^{-1}, while Fig. S6c and S6d show the corresponding curves at various current densities (1–10 A g^{-1}). As anticipated, the durations of charge and discharge shorten as current density increases, primarily due to constraints on ion transport and a decline in charge-storage efficiency, resulting in a steady reduction in specific capacity. Consistent with the CV and three-electrode measurements, the GONRs/Th (RT)//GONRs/Th (RT) device exhibits superior capacitive performance and faster charge

transfer than the HT-prepared system, confirming enhanced electrochemical reversibility and improved ion accessibility.

Fig. 5c illustrates the Nyquist diagrams obtained from electrochemical impedance spectroscopy of the symmetric two-electrode cells tested at open-circuit potential. The inset depicts the equivalent circuit employed for data fitting.[82] Both devices exhibit a small semicircular feature in the high-frequency range, indicative of charge-transfer resistance (R_{ct}), indicating limited impedance at the electrode/electrolyte interface. At lower frequencies, a Warburg process appears, reflecting ion diffusion within the porous electrode matrix. This diffusion-related response demonstrates that ion movement into the electrode bulk partly influences charge storage. Notably, the GONRs/Th (RT)//GONRs/Th (RT) device exhibits a steeper Warburg slope than the GONRs/Th (HT)//GONRs/Th (HT) device, suggesting lower ion-diffusion resistance and enhanced capacitive behavior.

Fig. 5d (Ragone plot) displays the interplay between energy density (E) and power density (P) for symmetric devices, based on GCD measurements at various current densities (1–10 A g^{-1}). At 1 A g^{-1}, the GONRs/Th (RT)//GONRs/Th (RT) and GONRs/Th (HT)//GONRs/Th (HT) supercapacitors achieve energy densities of 57 and 50 Wh kg^{-1}, with corresponding power densities of 873 and 857 W kg^{-1}. Increasing the current density to 10 A g^{-1} results in reduced energy densities of 22.8 and 24 Wh kg^{-1}, but significantly higher power densities of 8305 and 8680 W kg^{-1}. The superior energy and power performance of the GONRs/Th (RT)//GONRs/Th (RT) device can be ascribed to enhanced ion diffusion and redox processes, attributable to more effective integration of thionine within the GONR matrix. To facilitate a clear comparison with recent studies, Table 5 presents the energy and power densities of this work, along with data from representative and recent supercapacitor systems. This table highlights the device's competitive performance relative to previously reported materials under similar testing conditions.

The cycling stability of the symmetric devices was assessed through galvanostatic charge/discharge testing over 10 000 cycles. As shown in Fig. 5e and f, both devices demonstrated outstanding stability. The GONRs/Th (RT)//GONRs/Th (RT) device exhibited a gradual increase in capacitance to 111% after 2500 cycles, followed by stabilization at 102% after 10 000 cycles. The initial rise is attributed to electrode activation and ion-induced swelling, which enhances interlayer spacing and ion accessibility.[39,89] This device exhibited 100% capacitance retention through 5000 cycles, with 92% retention after 10 000 cycles. Both configurations showed a coulombic efficiency of approximately 98%, indicating excellent reversibility and durability over time. The enhanced rate performance and cycling stability are due to strong π–π interactions between thionine and GONRs, along with an interconnected microporous structure that enables rapid ion transport, effective electrolyte infiltration, and easy access to electroactive sites. The exceptional structural stability is due to the robust integration of thionine within the GONR framework, as previously confirmed by TGA data, which suppresses degradation mechanisms such as pore collapse or thionine detachment. Although thionine-based electrodes in acidic media often suffer from molecular degradation and leaching, compositing thionine with GONRs significantly improves structural integrity.[90] The conductive GONR ribbons provide abundant anchoring sites and strong π–π and amide-bonding interactions with thionine, effectively preventing dissolution and ensuring long-term stability. The inset images in Fig. 5e and f display cyclic voltammetry results for the devices tested at a scan rate of 100 mV s^{-1} after undergoing 3 and 10 000 galvanostatic charge–discharge cycles, thereby underscoring their stability. The electrodes exhibit a notably high specific capacitance, excellent retention of performance, and remarkable reversibility, demonstrating the potential of GONRs/Th composites as robust and reliable electrode materials for high-efficiency aqueous supercapacitors.

4.2. Electrocatalytic processes for hydrogen generation. The production of hydrogen *via* electrochemical water splitting relies heavily on the hydrogen evolution reaction. Enhancing the performance and activity of electrocatalysts is crucial to improving HER efficiency and advancing sustainable energy solutions.[91,92] Consequently, the electrochemical performance of GONRs and GONRs/Th composites as catalysts for the hydrogen evolution reaction was assessed by linear sweep voltammetry and electrochemical impedance spectroscopy in 1 M H_2SO_4, with a scan rate of 5 mV s^{-1}.

The LSV curves shown in Fig. 6a highlight varying catalytic performance across the tested electrodes. Overall, the GONRs/Th composites demonstrate improved hydrogen evolution reaction (HER) activity compared to pristine GONRs, with the GONRs/Th (HT) electrode exhibiting the highest efficiency, reaching a remarkably low overpotential of 122 mV at a current

Table 5 Comparison of energy and power density exhibited by thionine/carbon composite materials to the recent literature of similar materials

Electrodes	Electrolytes	Energy density (Wh kg^{-1})	Power density (W kg^{-1})	Ref.
Th–GA	1 M H_2SO_4	13.74	8.7	83
NRGO-H	2 M KOH	42.8	500	84
3D sponge nitrogen-doped graphene	6 M KOH	68.1	558.5	85
AgNP/rGO-cotton	PVA-H_2SO_4	34.6	125	86
NiO/GF	1 M KOH	32	700	87
rGO-cotton	PVA-H_3PO_4	27.05	—	88
GONRs/Th (RT)	1 M H_2SO_4	57	873	Current work
GONRs/Th (HT)	1 M H_2SO_4	50	857	Current work

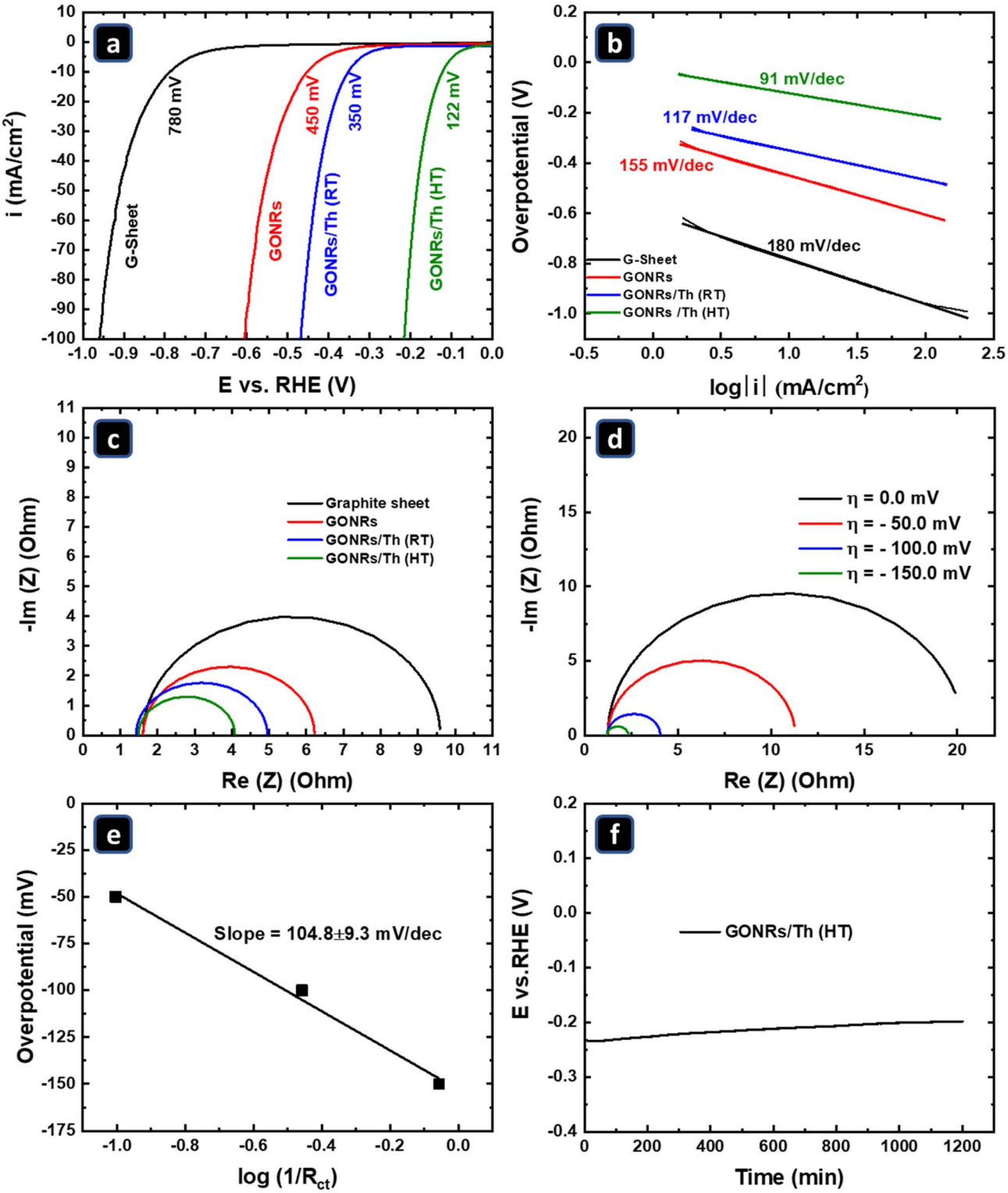

Fig. 6 Electrocatalyst HER activity was evaluated through various electrochemical methods: (a) linear sweep voltammetry at a scan rate of 5 mV s^{-1}, (b) Tafel slope analysis, (c) impedance spectroscopy Nyquist plots at fixed overpotential ($\eta = -100$ mV) for all electrodes, (d) impedance spectroscopy Nyquist plots at different overpotentials ($\eta = 0$ to -150 mV) for the GONRs/Th(HT) electrode, (e) relation between overpotential and log $1/R_{ct}$, and (f) chronopotentiometry measurements in a 1 M H_2SO_4 solution.

density of 10 mA cm^{-2} (η_{10}). The enhanced activity can be attributed to the intimate interaction between GONRs and thionine and the structural improvements introduced by hydrothermal treatment. These factors increase the density of active N and S sites, enhance charge-transfer kinetics, and improve structural stability, all of which are crucial for efficient

HER. The superior performance of the GONRs/Th (HT) composite underscores the vital role of the synthesis methodology in tailoring electrochemical properties for energy conversion applications.[91]

To better understand the reaction kinetics, Tafel plots were extracted from the LSV measurements (Fig. 6b). The GONRs/Th (HT) electrode shows the smallest Tafel slope of 91 mV dec^{-1}, which lies between the values for the Volmer (120 mV dec^{-1}) and Heyrovsky (40 mV dec^{-1}) steps. This suggests a combined Volmer–Heyrovsky mechanism, in which both hydrogen adsorption and electrochemical desorption contribute to the rate-limiting step. Similar intermediate slopes are commonly observed in heteroatom-doped carbon catalysts for the HER, indicating a suitable hydrogen binding affinity and balanced adsorption and desorption processes.[93–95] Y. Ito *et al.* showed that specific N–S configurations near lattice defects are crucial for achieving high HER activity. DFT calculations indicated that graphitic N atoms adjacent to S sites (–C–S–C– or –C═S–) form active centers with optimal hydrogen-adsorption free energies.[96] This configuration, part of the thionine structure, facilitates rapid electron transfer due to the combined electronic effects of the electron-withdrawing N and electron-donating S dopants.[96] In contrast, GONRs/Th (RT), pristine GONRs, and the bare graphite sheet exhibit higher slopes of 117, 155, and 180 mV dec^{-1}, respectively, corresponding to the V–H mechanism, with the Volmer step (hydrogen adsorption) being the rate-determining step.[93–95] The higher Tafel slope observed for the GONRs/Th (RT) electrode, compared with that of GONRs/Th (HT), can be attributed to the formation of local *p*–*n* junctions between the *n*-type thionine domains and the *p*-type GONR framework.[97,98] This interfacial doping causes charge redistribution and partial electron depletion around the N and S heteroatom sites, weakening hydrogen adsorption and thereby increasing the reaction overpotential. Following thermal treatment, partial removal of excess thionine and restoration of the π-conjugated network enhance electronic delocalization and improve conductivity. Consequently, the GONRs/Th (HT) electrode exhibits optimized hydrogen adsorption–desorption energetics, stronger electronic coupling between thionine and GONRs, and faster charge-transfer kinetics, collectively lowering the energy barrier for the HER.

To further investigate charge-transfer behavior during the hydrogen evolution reaction (HER), polarized electrochemical impedance spectroscopy (EIS) was conducted at −0.78 V *versus* MSE (−0.100 V *vs.* RHE). The selected potential for EIS measurements enables comparison of the catalytic abilities of all electrodes at the same minimal overpotential that retains responses in the kinetically controlled region and minimizes the influence of mass-transport limitations or excessive hydrogen bubble accumulation, which typically arises at higher overpotentials. An overpotential of −0.100 V *vs.* RHE is an intermediate overpotential within the kinetically controlled HER region rather than merely the onset potential or a mass-transport–dominated region. The results, presented in Fig. 6c, show that the GONRs/Th (HT) electrode has the smallest semicircle, indicating the lowest R_{ct}. This reduced R_{ct} indicates more rapid electron transfer and enhanced catalytic performance compared with other electrodes. These findings are consistent with linear sweep voltammetry (LSV) and Tafel slope data, supporting the conclusion that the hydrothermally synthesized electrode exhibits superior HER kinetics.

Extending EIS measurements over a broader overpotential range for the best electrode (GONRs/Th (HT)) could yield further insights into potential-dependent kinetic transitions or changes in the rate-determining step, enabling a more reliable comparison of intrinsic charge-transfer kinetics. Fig. 6d shows Nyquist plots of the EIS responses at different overpotentials (η = 0 to −150 mV) for the GONRs/Th (HT) electrode. A higher overpotential yields a less accurate R_{ct} value because the measured value is significantly smaller, and any error may lead to misinterpretation of the data. The R_{ct} decreases systematically with increasing overpotential, and a linear relationship between overpotential and $\log(1/R_{ct})$ with a Tafel slope of 104.8 ± 9.3 mV dec^{-1} is observed in Fig. 6e, reflecting the Volmer–Heyrovsky mechanism for the HER kinetics and supporting the results obtained from the analysis of the LSV measurements shown in Fig. 6b. When the R_{ct} value for zero overpotential was considered in the EIS-based Tafel slope calculation, the slope slightly increased to ≈ 117.7 ± 10.4 mV dec^{-1}, indicating a shift toward more domination by hydrogen adsorption as the rate-limiting step (Volmer mechanism) near the onset potential.

The durability of the GONRs/Th (HT) electrode was tested through chronopotentiometry at a current density of 50 mA cm^{-1} in a 1 M H_2SO_4 solution for a duration of 20 hours, as shown in Fig. 6f. A slight decrease in overpotential was observed, likely due to electrode activation over time and increased accessibility resulting from slight swelling during the testing process.[30] The minimal change in overpotential demonstrates excellent durability, attributed to the strong interaction between thionine and GONRs, which preserves structural integrity and retains conductivity. The synergistic combination of high conductivity, stable interfaces, and flexible architecture enables outstanding long-term HER performance, making the GONRs/Th (HT) composite a robust and efficient catalyst for practical hydrogen production.

5. Conclusion

This research introduces a simple and efficient method for producing thionine-coated graphene oxide nanoribbons (GONRs/Th) *via* both hydrothermal (HT) and ambient-temperature (RT) approaches. The resulting materials exhibit superior electrochemical qualities, indicating their potential for use in energy storage and conversion technologies. Structural and spectroscopic investigations confirm strong interactions between thionine and GONRs, which considerably enhance their electrical conductivity.

The GONRs/Th (RT) electrode exhibited notable pseudocapacitive behavior, reaching a specific capacitance (C_s) of 732 F g^{-1} at 1 A g^{-1}. Meanwhile, the GONRs/Th (HT) composite exhibited strong electrocatalytic performance for the HER, with an overpotential as low as 122 mV at 10 mA cm^{-2} and a Tafel slope of 91 mV per decade. Its remarkable stability, preserving both the structure and electrochemical properties for over 20

hours in 1 M H_2SO_4, was due to the effective π–π interactions and solid interfacial bonding between thionine and GONRs.

Overall, the synergistic effects of thionine incorporation and controlled synthesis conditions lead to enhanced charge transport, optimized active-site utilization, and improved mechanical stability. These findings position GONRs/Th composites as highly versatile and efficient candidates for next-generation supercapacitors, fuel cells, and hydrogen production technologies.

Conflicts of interest

There are no conflicts to declare.

Data availability

The data supporting this article have been included in the supplementary information (SI). Supplementary information: description of the SC device, TGA, Raman spectroscopy, electrochemical specific surface area calculation figures, CV curves at scan rates, and GCD curves at different current densities for three and two-electrode systems. See DOI: https://doi.org/10.1039/d6na00029k.

Acknowledgements

This research was supported by Emirates NBD, Sharjah Electricity, Water & Gas Authority (SEWA), and the Technology Innovation Institute (TII), which served as the principal sponsors of the 5th Forum for Women in Research (QUWA): Together Innovating to Shape the Future, held at the University of Sharjah (3656). The authors are grateful to the American University in Cairo for its continued funding and support.

References

1 E. Boateng, A. R. Thiruppathi, C.-K. Hung, D. Chow, D. Sridhar and A. Chen, Functionalization of Graphene-based Nanomaterials for Energy and Hydrogen Storage, *Electrochim. Acta*, 2023, **452**, 142340, DOI: 10.1016/j.electacta.2023.142340.

2 H. Alinajafi-Najafabadi, A. A. Ensafi and B. Rezaei, Reduced graphene oxide decorated with thionine, excellent nanocomposite material for a powerful electrochemical supercapacitor, *Int. J. Hydrogen Energy*, 2018, **43**, 19102–19110, DOI: 10.1016/j.ijhydene.2018.08.142.

3 L. Tingli, M. Ishtiaq, S. Saud and M. Q. Rasheed, Achieving sustainable development in emerging economies: Interplay between markets, resources, and environment, *Renewable Energy*, 2025, **238**, 121941, DOI: 10.1016/j.renene.2024.121941.

4 U. Shembade, R. Moholkar, S. Wategaonkar, P. Pillai, J. Khot and A. Moholkar, Tailoring the multifunctional properties of hydrothermally synthesized reduced graphene oxide/tungsten oxide supported nanorods to enhance the electrochemical and water-splitting activities, *Ceram. Int.*, 2024, **50**, 15044–15055, DOI: 10.1016/j.ceramint.2024.01.421.

5 A. Askarova, T. Alekhina, E. Popov, P. Afanasev, A. Mukhametdinova, A. Smirnov, A. Cheremisin and E. Mukhina, Innovative technology for underground clean *in situ* hydrogen generation: Experimental and numerical insights for sustainable energy transition, *Renew. Energy*, 2025, **240**, 122259, DOI: 10.1016/j.renene.2024.122259.

6 A. R. Heiba, M. O. Abdel-Salam, T. Yoon and E. E. Sawy, Aqueous supercapacitors with ultrawide potential window and pH independent stability using electrodes of graphene oxide nanoribbons/Fe-MOFs nanocomposite, *Chem. Eng. J.*, 2025, **516**, 164012, DOI: 10.1016/j.cej.2025.164012.

7 A. R. Heiba, M. O. Abdel-Salam, T. Yoon and E. El Sawy, Zr-MOF composites with zipped and unzipped carbon nanotubes for high-performance electrochemical supercapacitors, *Nanoscale*, 2024, 459–473, DOI: 10.1039./D4NR03926B.

8 Y. Shabangoli, M. Rahmanifar, M. El-Kady, A. Noori, M. Mousavi and R. Kaner, Thionine Functionalized 3D Graphene Aerogel: Combining Simplicity and Efficiency in Fabrication of a Metal-Free Redox Supercapacitor, *Adv. Energy Mater.*, 2018, **8**, 1802869–1802881, DOI: 10.1002/aenm.201802869.

9 M. Bhosale, T. Sadhasivam, N. Murugan, Y. Kim and T. Oh, Engineering 2D heterostructured VS 2 -rGO-Ni nanointerface to stimulate electrocatalytic water splitting and supercapacitor applications, *J. Energy Storage*, 2023, **73**, 109133, DOI: 10.1016/j.est.2023.109133.

10 H. Zhang, B. Farhadi, K. Wang, X. Xing, K. Wang and S. L. Frank Liu, Electrostatically Anchored Mxene-Thionine Hybrid Electrodes Prepared in *Situ for a Flexible Supercapacitor to Attain Exceptional Performance*, 2023. doi: DOI: 10.2139/ssrn.4556629.

11 H. Kye, Y. Kang, D. Jang, J. Kwon and B.-G. Kim, -Type Redox-Active Organic Electrode Materials for Next-Generation Rechargeable Batteries, *Adv. Energy Sustain. Res.*, 2022, **3**, 2200030–2200056, DOI: 10.1002/aesr.202200030.

12 C. Luo, O. Borodin, X. Ji, S. Hou, K. Gaskell, X. Fan, J. Chen, T. Deng, R. Wang, J. Jiang and C. Wang, Azo compounds as a family of organic electrode materials for alkali-ion batteries, *Proc. Natl. Acad. Sci. U. S. A.*, 2018, **115**, 201717892, DOI: 10.1073/pnas.1717892115.

13 C. Luo, G.-L. Xu, X. Ji, S. Hou, L. Chen, F. Wang, J. Jiang, Z. Chen, Y. Ren, K. Amine and C. Wang, Reversible Redox Chemistry of Azo Compounds for Sodium Ion Batteries, *Angew. Chem., Int. Ed.*, 2018, **57**, 2879–2883, DOI: 10.1002/anie.201713417.

14 Q. Zhao, W. Huang, Z. Luo, L. Liu, Y. Lu, Y. Li, L. Li, J. Hu, H. Ma and J. Chen, High-capacity aqueous zinc batteries using sustainable quinone electrodes, *Sci. Adv.*, 2018, **4**, eaao1761, DOI: 10.1126/sciadv.aao1761.

15 Y. Liu, X. Zhao, C. Fang, Q. Liu, Y. Huang, R. Zeng, K. Litao, J. Liu and Y. Huang, Activating Aromatic Rings as Na-Ion Storage Sites to Achieve High Capacity, *SSRN Electron. J.*, 2018, 2463–2478, DOI: 10.2139/ssrn.3155704.

16 Y. Lu, X. Hou, L. Miao, L. Li, R. Shi, L. Liu and J. Chen, Cyclohexanehexone with Ultrahigh Capacity as Cathode

Materials for Lithium-Ion Batteries, *Angew. Chem.*, 2019, **131**, 7020–7024, DOI: 10.1002/ange.201902185.

17 Z. Song, L. Miao, H. Duan, L. Ruhlmann, Y. Lv, D. Zhu, L. Gan and M. Liu, Anionic Co-insertion Charge Storage in Dinitrobenzene Cathodes for High-Performance Aqueous Zinc–Organic Batteries, *Angew. Chem., Int. Ed.*, 2022, **61**, e202208821–e202208831, DOI: 10.1002/anie.202208821.

18 N. Wang, Z. Guo, Z. Ni, J. Xu, X. Qiu, J. Ma, P. Wei and Y. Wang, Molecular Tailoring of an n/p-type Phenothiazine Organic Scaffold for Zinc Batteries, *Angew. Chem., Int. Ed.*, 2021, **60**, 20826–20832, DOI: 10.1002/anie.202106238.

19 S. Pengfei, Q. Chen, D.-Y. Wang, W. Guo and Y. Fu, Organosulfur Materials for Rechargeable Batteries: Structure, Mechanism, and Application, *Chem. Rev.*, 2023, **123**, 1207–1840, DOI: 10.1021/acs.chemrev.2c00739.

20 Z. Wang, H. Jiang, Y. Zhang, Y. An, C. Wei, L. Tan, S. Xiong, Y. Qian and J. Feng, Application of 2D MXene in Organic Electrode Materials for Rechargeable Batteries: Recent Progress and Perspectives, *Adv. Funct. Mater.*, 2023, **33**, 2210184–2210198, DOI: 10.1002/adfm.202210184.

21 Y. Zhang, Y. Wang, C. Gao, Z. Ni, X. Zhang, W. Hu and H. Dong, Recent advances in n-type and ambipolar organic semiconductors and their multi-functional applications, *Chem. Soc. Rev.*, 2023, **52**, 1331–1381, DOI: 10.1039/D2CS00720G.

22 Y. Zhu, G. Yang, X. Wan, J. Deng, T. Burton, S. Deebansok, D. Zigah, H. Zhou, Y. Guo and O. Fontaine, Exploring the Role of Redox Mediator within Mesoporous Carbon Using Thionine and LiTFSI Water-in-Salt Electrolytes, *Energy Storage Mater.*, 2022, **55**, 808–815, DOI: 10.1016/j.ensm.2022.12.026.

23 A. Shi, F. Qu, H. Ming, G. Shen and R. Yu, Amperometric H2O2 biosensor based on poly-thionine nanowire/HRP/nano-Au-modified glassy carbon electrode, *Sens. Actuators, B Chem.*, 2008, **129**, 779–783, DOI: 10.1016/j.snb.2007.09.062.

24 J. Kang, O. Kwon, J. P. Kim, J. Y. Kim, J. Kim, Y. Cho and D. W. Kim, Graphene Membrane for Water-Related Environmental Application: A Comprehensive Review and Perspectives, *ACS Environ. Au*, 2025, **5**, 35–60, DOI: 10.1021/acsenvironau.4c00088.

25 H. Zhang, B. Farhadi, K. Wang, X. Xing, K. Wang and S. L. Frank Liu, Electrostatically Anchored Mxene-Thionine Hybrid Electrodes Prepared in *Situ for a Flexible Supercapacitor to Attain Exceptional Performance*, 2023. doi: DOI: 10.2139/ssrn.4556629.

26 A. R. Heiba, F. A. Taher, R. M. Abou Shahba and N. A. Abdel Ghany, Corrosion mitigation of carbon steel in acidic and salty solutions using electrophoretically deposited graphene coatings, *J. Coat. Technol. Res.*, 2021, **18**, 501–510, DOI: 10.1007/s11998-020-00419-z.

27 Y. Cai, Y. Wang, L. Cheng, S. Guo, T. Liu, Z. Hu, H. Yu, D. Chen, Y. Li and H. Yuan, Structure design and assembly mode of carbon nanotube-based flexible electrode materials and flexible supercapacitors, *J. Energy Storage*, 2023, **73**, 109179, DOI: 10.1016/j.est.2023.109179.

28 B. Wan, H. Zhang, S. Tang, S. Li, Y. Wang, D. Wen, M. Zhang and Z. Li, High-sulfur-doped hard carbon for sodium-ion battery anodes with large capacity and high initial coulombic efficiency, *Sustain. Energy Fuels*, 2022, **6**, 4338–4345, DOI: 10.1039/D2SE00937D.

29 R. Vicentini, W. G. Nunes, L. H. da Costa, L. M. Da Silva, B. Freitas, A. M. Pascon, O. Vilas-Boas and H. Zanin, Multi-walled carbon nanotubes and activated carbon composite material as electrodes for electrochemical capacitors, *J. Energy Storage*, 2021, **33**, 100738, DOI: 10.1016/j.est.2019.04.012.

30 A. R. Heiba, R. M. Abou Shahba, A. S. Dhmees, F. A. Taher and E. N. El Sawy, Graphene oxide nanoribbons (GONRs) as pH-tolerant electrodes for supercapacitors: Effect of charge carriers and loading, *J. Energy Storage*, 2024, **83**, 110762, DOI: 10.1016/j.est.2024.110762.

31 A. R. Heiba, M. O. Abdel-Salam, T. Yoon and E. E. Sawy, Zr-MOF composites with zipped and unzipped carbon nanotubes for high-performance electrochemical supercapacitors, *Nanoscale*, 2025, **17**, 459–473, DOI: 10.1039/D4NR03926B.

32 R. Houtsma, J. Rie and M. Stöhr, Atomically precise graphene nanoribbons: interplay of structural and electronic properties, *Chem. Soc. Rev.*, 2021, **50**, 6541–6568, DOI: 10.1039/D0CS01541E.

33 M. G. Ersozoglu, H. Gursu, S. Gumrukcu, A. S. Sarac and Y. Sahin, Single Step Electrochemical Semi-Exfoliated S-Doped Graphene-Like Structures from Commercial Carbon Fiber as Efficient Metal-Free Catalyst for Hydrogen Evolution Reaction, *Chemelectrochem*, 2022, **9**, e202101455, DOI: 10.1002/celc.202101455.

34 W. Zheng, Y. Zhang, K. Niu, T. Liu, K. Bustillo, P. Ercius, D. Nordlund, J. Wu, H. Zheng and X. Du, Selective nitrogen doping of graphene oxide by laser irradiation for enhanced hydrogen evolution activity, *Chem. Commun.*, 2018, **54**, 13726–13729, DOI: 10.1039/C8CC07725H.

35 X. Liu, W. Zhou, L. Yang, L. Li, Z. Zhang, Y. Ke and S. Chen, Nitrogen and sulfur co-doped porous carbon derived from human hair as highly efficient metal-free electrocatalysts for hydrogen evolution reactions, *J. Mater. Chem. A*, 2015, **3**, 8840–8846, DOI: 10.1039/C5TA01209K.

36 D. Kosynkin, A. Higginbotham, A. Sinitskii, J. Lomeda, A. Dimiev, B. Price and J. Tour, Longitudinal Unzipping of Carbon Nanotubes to Form Graphene Nanoribbons, *Nature*, 2009, **458**, 872–876, DOI: 10.1038/nature07872.

37 B. Zhang, Z. Wen, S. Ci, J. Chen and Z. He, *Nitrogen-doped Activated Carbon as a Metal Free Catalyst for Hydrogen Production in Microbial Electrolysis Cells*, 2014. DOI: 10.1039/C4RA08555H.

38 J. Kusuma, R. G. Balakrishna, S. Patil, M. S. Jyothi, H. R. Chandan and R. Shwetharani, Exploration of graphene oxide nanoribbons as excellent electron conducting network for third generation solar cells, *Sol. Energy Mater. Sol. Cells*, 2018, **183**, 211–219, DOI: 10.1016/j.solmat.2018.01.039.

39 A. R. Heiba, R. M. Abou Shahba, A. S. Dhmees, F. A. Taher and E. N. El Sawy, Graphene oxide nanoribbons (GONRs)

as pH-tolerant electrodes for supercapacitors: Effect of charge carriers and loading, *J. Energy Storage*, 2024, **83**, 110762, DOI: 10.1016/j.est.2024.110762.

40 D. S. Dkhar, R. Kumari and P. Chandra, Chemically engineered unzipped multiwalled carbon nanotube and rGO nanohybrid for ultrasensitive picloram detection in rice water and soil samples, *Sci. Rep.*, 2023, **13**, 9899, DOI: 10.1038/s41598-023-34536-7.

41 T. A. S. L. De Sousa, T. F. D. Fernandes, M. J. S. Matos, E. N. D. Araujo, M. S. C. Mazzoni, B. R. A. Neves and F. Plentz, Thionine Self-Assembled Structures on Graphene: Formation, Organization, and Doping, *Langmuir*, 2018, **34**, 6903–6911, DOI: 10.1021/acs.langmuir.8b00506.

42 J. Zhao, Y. Deng, H. Wei, X. Zheng, Z. Yu, Y. Shao, J. E. Shield and J. Huang, Strained hybrid perovskite thin films and their impact on the intrinsic stability of perovskite solar cells, *Sci. Adv.*, 2017, **3**, eaao5616, DOI: 10.1126/sciadv.aao5616.

43 Q. Zhou, G. Li, Y. Zhang, M. Zhu, Y. Wan and Y. Shen, Highly Selective and Sensitive Electrochemical Immunoassay of Cry1C Using Nanobody and π–π Stacked Graphene Oxide/Thionine Assembly, *Anal. Chem.*, 2016, **88**, 9830–9836, DOI: 10.1021/acs.analchem.6b02945.

44 N. Choudhary, C. Li, J. Moore, N. Nagaiah, L. Zhai, Y. Jung and J. Thomas, Asymmetric Supercapacitor Electrodes and Devices, *Adv. Mater.*, 2017, **29**, 1605336, DOI: 10.1002/adma.201605336.

45 J. Zhao and A. Burke, Electrochemical Capacitors: Performance Metrics and Evaluation by Testing and Analysis, *Adv. Energy Mater.*, 2020, **11**, 2002192, DOI: 10.1002/aenm.202002192.

46 J. Li, J. Guo and H. Dai, Probing dissolved CO2(aq) in aqueous solutions for CO2 electroreduction and storage, *Sci. Adv.*, 2022, **8**, eabo0399, DOI: 10.1126/sciadv.abo0399.

47 M. El-Kady, M. Bierwirth, M. Li, J. Hwang, M. Mousavi, L. Chaney, A. Lech and R. Kaner, Engineering three-dimensional hybrid supercapacitors and microsupercapacitors for high-performance integrated energy storage, *Proc. Natl. Acad. Sci. U. S. A.*, 2015, **112**, 4233–4238, DOI: 10.1073/pnas.1420398112.

48 P. Kakvand, M. Rahmanifar, M. El-Kady, A. Pendashteh, M. A. Kiani, M. Hashemi, M. Najafi, A. Abbasi, M. Mousavi and R. Kaner, Synthesis of NiMnO3/C nano-composite electrode materials for electrochemical capacitors, *Nanotechnology*, 2016, **27**, 315401, DOI: 10.1088/0957-4484/27/31/315401.

49 M. A. Ibrahim, N. A. M. Jani, O. H. Hassan, F. Abdullah, T. I. T. Kudin, A. M. M. B. Ali and M. Z. A. Yahya, FTIR Spectrum Investigation of Thionine-Graphene Nanocomposite, *Appl. Mech. Mater.*, 2017, **864**, 42–47, DOI: 10.4028/www.scientific.net/AMM.864.42.

50 E. Krzyszkowska, J. Walkowiak-Kulikowska, S. Stienen and A. Wojcik, Thionine–graphene oxide covalent hybrid and its interaction with light, *Phys. Chem. Chem. Phys.*, 2017, **19**, 14412–14423, DOI: 10.1039/C7CP01267E.

51 B. Ossonon and D. Bélanger, Synthesis and characterization of sulfophenyl-functionalized reduced graphene oxide sheets, *RSC Adv.*, 2017, **7**, 27224–27234, DOI: 10.1039/C6RA28311J.

52 M. F. El-Kady, Y. Shao and R. B. Kaner, Graphene for batteries, supercapacitors and beyond, *Nat. Rev. Mater.*, 2016, **1**, 1–14, DOI: 10.1038/natrevmats.2016.33.

53 Z. Li, L. Deng, I. A. Kinloch and R. J. Young, Raman spectroscopy of carbon materials and their composites: Graphene, nanotubes and fibres, *Prog. Mater. Sci.*, 2023, **135**, 101089, DOI: 10.1016/j.pmatsci.2023.101089.

54 D. B. Schuepfer, F. Badaczewski, J. M. Guerra-Castro, D. M. Hofmann, C. Heiliger, B. Smarsly and P. J. Klar, Assessing the structural properties of graphitic and non-graphitic carbons by Raman spectroscopy, *Carbon*, 2020, **161**, 359–372, DOI: 10.1016/j.carbon.2019.12.094.

55 A. L. Higginbotham, D. V. Kosynkin, A. Sinitskii, Z. Sun and J. M. Tour, Lower-Defect Graphene Oxide Nanoribbons from Multiwalled Carbon Nanotubes, *ACS Nano*, 2010, **4**, 2059–2069, DOI: 10.1021/nn100118m.

56 M. D. Bhatt, H. Kim and G. Kim, Various defects in graphene: a review, *RSC Adv.*, 2022, **12**, 21520–21547, DOI: 10.1039/D2RA01436J.

57 K. Hutchinson, R. E. Hester, W. J. Albery and A. R. Hillman, Raman spectroscopic studies of a thionine-modified electrode, *J. Chem. Soc. Faraday Trans. 1 Phys. Chem. Condens. Phases*, 1984, **80**, 2053, DOI: 10.1039/f19848002053.

58 C. Qiu, L. Jiang, Y. Gao and L. Sheng, Effects of oxygen-containing functional groups on carbon materials in supercapacitors: A review, *Mater. Des.*, 2023, **230**, 111952, DOI: 10.1016/j.matdes.2023.111952.

59 J. Cui, S. Yao, Z. Lu, J.-Q. Huang, W. G. Chong, F. Ciucci and J.-K. Kim, Revealing Pseudocapacitive Mechanisms of Metal Dichalcogenide SnS 2/Graphene-CNT Aerogels for High-Energy Na Hybrid Capacitors, *Adv. Energy Mater.*, 2017, **8**, 1702488, DOI: 10.1002/aenm.201702488.

60 W. Zuo, R. Li, C. Zhou, Y. Li, J. Xia and J. Liu, Battery-Supercapacitor Hybrid Devices: Recent Progress and Future Prospects, *Adv. Sci.*, 2017, **4**, 1600539, DOI: 10.1002/advs.201600539.

61 M. Hashemi, M. Rahmanifar, M. El-Kady, A. Noori, M. Mousavi and R. Kaner, The Use of an Electrocatalytic Redox Electrolyte for Pushing the Energy Density Boundary of a Flexible Polyaniline Electrode to a New Limit, *Nano Energy*, 2017, **44**, 489–498, DOI: 10.1016/j.nanoen.2017.11.058.

62 W. Hou, X.-Z. Yuan, Y. Wu, G. Zeng, X. Chen, L. Leng, Z. Wu, L. Jiang and H. Li, Facile synthesis of amino-functionalized titanium metal-organic frameworks and their superior visible-light photocatalytic activity for Cr(VI) reduction, *J. Hazard. Mater.*, 2015, **286**, 187–194, DOI: 10.1016/j.jhazmat.2014.11.039.

63 P. Balakrishnan, Volatility of amines used for water treatment in steam generating systems, *Can. J. Chem.*, 2011, **56**, 2620–2623, DOI: 10.1139/v78-431.

64 T. Xiong, W. S. V. Lee, L. Chen, T. Tan, X. Huang and J. Xue, Indole-Based Conjugated Macromolecule as Redox-Mediated Electrolyte for Ultrahigh Power Supercapacitor,

Energy Sci. Eng., 2017, **10**, 2441–2449, DOI: 10.1039/C7EE02584J.

65 Y. Wu, T. Momma, S. Ahn, T. Yokoshima, H. Nara and T. Osaka, On-site chemical pre-lithiation of S cathode at room temperature on a 3D nano-structured current collector, *J. Power Sources*, 2017, **366**, 65–71, DOI: 10.1016/j.jpowsour.2017.08.113.

66 Z. Chen, Y. Liu, L. Hao, Z. Zhu, F. Li and S. Liu, Reduced Graphene Oxide-Zirconium Dioxide–Thionine Nanocomposite Integrating Recognition, Amplification, and Signaling for an Electrochemical Assay of Protein Kinase Activity and Inhibitor Screening, *ACS Appl. Bio Mater.*, 2018, **1**, 1557–1565, DOI: 10.1021/acsabm.8b00451.

67 Y. Shabangoli, M. Rahmanifar, M. El-Kady, A. Noori, M. Mousavi and R. Kaner, Thionine Functionalized 3D Graphene Aerogel: Combining Simplicity and Efficiency in Fabrication of a Metal-Free Redox Supercapacitor, *Adv. Energy Mater.*, 2018, **8**, 1802869–1802871, DOI: 10.1002/aenm.201802869.

68 A label-free electrochemical DNA biosensor based on thionine functionalized reduced graphene oxide, *Carbon* **129** (2018) 730–737. doi: DOI: 10.1016/j.carbon.2017.12.060.

69 R. Kumar and M. Bag, Quantifying Capacitive and Diffusion-Controlled Charge Storage from 3D Bulk to 2D Layered Halide Perovskite-Based Porous Electrodes for Efficient Supercapacitor Applications, *J. Phys. Chem. C*, 2021, **125**, 16946–16954, DOI: 10.1021/acs.jpcc.1c05493.

70 S. Zeng, H. Chen, F. Cai, Y. Kang, M. Chen and Q. Li, Electrochemical fabrication of carbon nanotube/polyaniline hydrogel film for all-solid-state flexible supercapacitor with high areal capacitance, *J. Mater. Chem. A*, 2015, **3**, 23864–23870, DOI: 10.1039/C5TA05937B.

71 A. R. Heiba, R. M. Abou Shahba, A. S. Dhmees, F. A. Taher and E. N. El Sawy, Graphene oxide nanoribbons (GONRs) as pH-tolerant electrodes for supercapacitors: Effect of charge carriers and loading, *J. Energy Storage*, 2024, **83**, 110762, DOI: 10.1016/j.est.2024.110762.

72 B. Song, C.-C. Tuan, X. Huang, L. Li, K. Moon and C. P. Wong, Sulfonated Polyaniline Decorated Graphene Nanocomposites as Supercapacitor Electrodes, *Mater. Lett.*, 2015, **166**, 12–15, DOI: 10.1016/j.matlet.2015.11.108.

73 C. Liu, G. Han, Y. Chang, Y. Xiao, H. Zhou and G. Shi, High-performance supercapacitors based on the reduced graphene oxide hydrogels modified by trace amounts of benzenediols, *Chem. Eng. J.*, 2017, **328**, 25–34, DOI: 10.1016/j.cej.2017.07.032.

74 L. Wan, C. Du and S. Yang, Synthesis of graphene oxide/polybenzoxazine-based nitrogen-containing porous carbon nanocomposite for enhanced supercapacitor properties, *Electrochim. Acta*, 2017, **251**, 12–24, DOI: 10.1016/j.electacta.2017.08.086.

75 K. Krishnamoorthy, S. Thangavel, J. Chelora Veetil, N. Raju, G. Venugopal and S. J. Kim, Graphdiyne nanostructures as a new electrode material for electrochemical supercapacitors, *Int. J. Hydrogen Energy*, 2016, **41**, 1672–1678, DOI: 10.1016/j.ijhydene.2015.10.118.

76 M. Demir, B. Ashourirad, J. H. Mugumya, S. K. Saraswat, H. M. El-Kaderi and R. B. Gupta, Nitrogen and oxygen dual-doped porous carbons prepared from pea protein as electrode materials for high performance supercapacitors, *Int. J. Hydrogen Energy*, 2018, **43**, 18549–18558, DOI: 10.1016/j.ijhydene.2018.03.220.

77 L. Sui, Y. Wang, W. Ji, H. Kang, L. Dong and L. Yu, N-doped ordered mesoporous carbon/graphene composites with supercapacitor performances fabricated by evaporation induced self-assembly, *Int. J. Hydrogen Energy*, 2017, **42**, 29820–29829, DOI: 10.1016/j.ijhydene.2017.10.113.

78 D. Wang, Y. Min, Y. Yu and B. Peng, A general approach for fabrication of nitrogen-doped graphene sheets and its application in supercapacitors, *J. Colloid Interface Sci.*, 2014, **417**, 270–277, DOI: 10.1016/j.jcis.2013.11.021.

79 B.-A. Mei, O. Munteshari, J. Lau, B. Dunn and L. Pilon, Physical Interpretations of Nyquist Plots for EDLC Electrodes and Devices, *J. Phys. Chem. C*, 2017, **122**, 194–206, DOI: 10.1021/acs.jpcc.7b10582.

80 A. Tyagi, K. Mishra, S. Sharma and V. Shukla, Performance studies of an electric double-layer capacitor (EDLC) fabricated using edible oil-derived activated carbon, *J. Mater. Sci. Mater. Electron.*, 2021, **33**, 1–15, DOI: 10.1007/s10854-021-06978-0.

81 S. Myeong, S. Ha, C. Lim, C. G. Min and Y.-S. Lee, Effect of fluorine functional groups introduced into activated carbon aerogel by carbon tetrafluoride plasmas in supercapacitors, *Carbon Lett.*, 2023, **34**, 65–74, DOI: 10.1007/s42823-023-00668-z.

82 B. Vidyadharan, R. A. Aziz, I. I. Misnon, G. M. Anil Kumar, J. Ismail, M. M. Yusoff and R. Jose, High energy and power density asymmetric supercapacitors using electrospun cobalt oxide nanowire anode, *J. Power Sources*, 2014, **270**, 526–535, DOI: 10.1016/j.jpowsour.2014.07.134.

83 Y. Shabangoli, M. Rahmanifar, A. Noori, M. Mousavi and R. Kaner, Thionine Functionalized 3D Graphene Aerogel: Combining Simplicity and Efficiency in Fabrication of a Metal-Free Redox Supercapacitor, *Adv. Energy Mater.*, 2018, **8**, 1802869–1802871, DOI: 10.1002/aenm.201802869.

84 P. Bharathidasan, M. B. Idris, D.-W. Kim, S. R. Sivakkumar and S. Devaraj, Enhanced capacitance properties of nitrogen doped reduced graphene oxide obtained by simultaneous reduction and nitrogen doping, *FlatChem*, 2018, **11**, 24–31, DOI: 10.1016/j.flatc.2018.10.001.

85 N. A. Elessawy, J. El Nady, W. Wazeer and A. B. Kashyout, Development of High-Performance Supercapacitor based on a Novel Controllable Green Synthesis for 3D Nitrogen Doped Graphene, *Sci. Rep.*, 2019, **9**, 1129, DOI: 10.1038/s41598-018-37369-x.

86 Z. Karami, M. Youssefi, K. Raeissi and M. Zhiani, An efficient textile-based electrode utilizing silver nanoparticles/reduced graphene oxide/cotton fabric composite for high-performance wearable supercapacitors, *Electrochim. Acta*, 2021, **368**, 137647, DOI: 10.1016/j.electacta.2020.137647.

87 H. Wang, H. Yi, X. Chen and X. Wang, Asymmetric supercapacitors based on nano-architectured nickel oxide/graphene foam and hierarchical porous nitrogen-doped

carbon nanotubes with ultrahigh-rate performance, *J. Mater. Chem. A*, 2014, **2**, 3223–3230, DOI: 10.1039/C3TA15046A.

88 Y. Li, Y. Zhang, H. Zhang, T. Xing and G. Chen, A facile approach to prepare a flexible sandwich-structured supercapacitor with rGO-coated cotton fabric as electrodes, *RSC Adv.*, 2019, **9**, 4180–4189, DOI: 10.1039/C9RA00171A.

89 A. Iakunkov, A. Nordenström, N. Boulanger, G. Li, C. Hennig, M. R. V. Jørgensen, I. Kantor and A. V. Talyzin, Effect of Chain Length on Swelling Transitions of Brodie Graphite Oxide in Liquid 1-Alcohols, *Adv. Mater. Interfaces*, 2024, **11**, 2300554, DOI: 10.1002/admi.202300554.

90 Y. Shabangoli, M. S. Rahmanifar, M. F. El-Kady, A. Noori, M. F. Mousavi and R. B. Kaner, Thionine Functionalized 3D Graphene Aerogel: Combining Simplicity and Efficiency in Fabrication of a Metal-Free Redox Supercapacitor, *Adv. Energy Mater.*, 2018, **8**, 1802869, DOI: 10.1002/aenm.201802869.

91 G. Zhao, K. Rui, S. X. Dou and W. Sun, Heterostructures for Electrochemical Hydrogen Evolution Reaction: A Review, *Adv. Funct. Mater.*, 2018, **28**, 1803291, DOI: 10.1002/adfm.201803291.

92 A. R. Heiba, M. M. Omran, S. E. Abd El Hamid, N. K. Allam and E. N. El Sawy, Surface Engineering of Stainless-Steel 316L and 304L Electrodes for Hydrogen Production in Alkaline and Saline Water, *Energy Fuels*, 2024, **38**, 22424–22439, DOI: 10.1021/acs.energyfuels.4c03280.

93 G. Long, K. Wan, M. Liu, Z. Liang, J. Piao and P. Tsiakaras, Active sites and mechanism on nitrogen-doped carbon catalyst for hydrogen evolution reaction, *J. Catal.*, 2017, **348**, 151–159, DOI: 10.1016/j.jcat.2017.02.021.

94 M. Cai, L. Xu, J. Guo, X. Yang, X. He and P. Hu, Recent advances in metal-free electrocatalysts for the hydrogen evolution reaction, *J. Mater. Chem. A*, 2024, **12**, 592–612, DOI: 10.1039/D3TA05901D.

95 A. Lasia, Mechanism and kinetics of the hydrogen evolution reaction, *Int. J. Hydrogen Energy*, 2019, **44**, 19484–19518, DOI: 10.1016/j.ijhydene.2019.05.183.

96 Y. Ito, W. Cong, T. Fujita, Z. Tang and M. Chen, High Catalytic Activity of Nitrogen and Sulfur Co-Doped Nanoporous Graphene in the Hydrogen Evolution Reaction, *Angew. Chem., Int. Ed.*, 2015, **54**, 2131–2136, DOI: 10.1002/anie.201410050.

97 T. A. S. L. Sousa, F. A. Santos, T. G. Silva, E. N. D. Araujo and F. Plentz, Surface modification of graphene with thionine: Formation of *p–n* junctions, *Appl. Surf. Sci.*, 2020, **530**, 147003, DOI: 10.1016/j.apsusc.2020.147003.

98 D.-T. Phan and G.-S. Chung, P–n junction characteristics of graphene oxide and reduced graphene oxide on n-type Si(111), *J. Phys. Chem. Solids*, 2013, **74**, 1509–1514, DOI: 10.1016/j.jpcs.2013.02.007.